Computationally-Efficient High-Fidelity Nonlinear FEA of Seismically Isolated Post-Tensioned RC Bridges

George Markou, Ph.D., P.Eng.[1] and Mohammad AlHamaydeh, Ph.D., P.E., F.SEI[2]

ABSTRACT

This study presents a novel computationally efficient high-fidelity nonlinear FEA (NLFEA) methodology for prestressed RC bridges constructed in the UAE and seismically isolated with elastomeric bearings. Specifically, the presented NLFEA methodology, using 3D solid brick elements, is shown to overcome traditional prohibitive numerical burdens. This is demonstrated without compromising accuracy or upscaling applicability and appropriateness. The proposed NLFEA approach is highlighted through detailed modeling of RC bridges' non-traditional structural components and loading aspects (elastomeric bearings and post-tension prestressing cables). The mechanical behavior of elastomeric isolators and the RC continua, including cracking and other nonlinear phenomena, are captured via 3D solid brick elements. Moreover, the modeling procedure accurately represents the post-tension tendons' prestressing forces and the associated effects on the RC elements. The prestressing forces are incorporated within the tendon elements via insightful manipulations of stepwise initial conditions and internal force adjustments. Additionally, load-carrying capacity determination for the elastomeric bearings was achieved by conducting a parametric investigation to capture their mechanical behavior adequately. Eventually, the analysis of a full-scale bridge is presented in this paper. The post-tensioned RC bridge understudy spans 100m over eight elastomeric (natural rubber) seismic isolator bearings. Twelve post-tension prestressing cables are utilized to provide the bridge with continuous internal tension-balancing forces. A high-fidelity detailed FEA model of the complete bridge is developed and validated against a SAP2000 FEA model. It is shown that reasonable computational efforts can be expected without compromising the accuracy of the results.

Keywords: Full-Scale Bridge Modeling, Simulation, Nonlinear Analysis Finite Element Analysis (NLFEA), Prestressing, Elastomeric Bearing.

1 Introduction

The mechanical behavior of RC bridges is commonly assessed in terms of ductility and maximum load-carrying capacity. Nevertheless, modeling and analyzing RC bridges pose significant challenges for researchers and FEA software developers. These challenges stem from the inherent complexity of bridge components and vast geometry, along with the inevitable associated computational burdens. As a result, numerical analysis of RC bridges is often computationally prohibitive, especially for full-scale models where 3D continuity considerations are of the essence. It is widely accepted that detailed 3D FE models are the most likely method to reach the most accurate numerical representations of physical phenomena. Such complex phenomena which characterize mechanical behavior are often otherwise inaccessible due to the high cost of thorough destructive experimental investigations.

Several methods have been proposed to assess the mechanical behavior of RC bridges under earthquake loads in accordance with provisions from the Eurocode [1] and AASHTO [2]. The main approaches were: modal pushover analysis, linear dynamic analysis, and linear static analysis [3]. It is common practice to utilize beam-column elements and 2D finite elements (i.e., shell elements) to study the mechanical behavior of bridges. In doing so, researchers employ a series of material and geometrical assumptions to investigate RC bridges' overall dynamic and nonlinear behaviors [4]–[18]. These simplified models are typically sufficient for holistic structural analysis. However, they lack the necessary tools to account for localized

---

[1] Associate Professor, Department of Civil Engineering, University of Pretoria, South Africa, george.markou@up.ac.za

[2] Corresponding author: Professor, Department of Civil Engineering, College of Engineering, American University of Sharjah, Sharjah, PO Box 26666, UAE; malhamaydeh@aus.edu , ORCID ID: 0000-0002-5004-0778.

nonlinear phenomena such as cracking, rebar yielding, or 3D mechanical behavior of elastomeric bearings, not to mention the interactions between individual structural components (e.g., bearings, deck, piers, and abutments, etc.).

As Kappos et al. [6] discussed, the past two decades witnessed a shift in research interests towards performance-based analysis and design approaches. This involved obtaining inelastic deformations through elaborate nonlinear numerical simulations and thus re-highlighting the need for accurate nonlinear modeling. As a result, several researchers began employing 2D and 3D detailed modeling of independent structural components of RC bridges (e.g. [19]–[28]). Furthermore, research efforts have enabled the complete and thorough modeling of bridge geometry to allow for accurate nonlinear analysis [29]–[35].

For instance, Mwafy et al. [34] proposed an idealization methodology foreseeing the modeling of the A-1700 bridge at Caruthersville through SAP2000 [35] and Zeus NL [36]. The super-structure of the bridge was modeled with beam-column elements and the sub-structure with cubic elastoplastic elements. The soil domain was also incorporated into their numerical model. Their research's focus on describing a realistic idealization procedure highlights the importance of simulating large-scale structures with detailed 3D models accounting for material and geometric nonlinearities.

Using ATENA, Richard et al. [19] modeled a 50-year-old concrete trough bridge with 2D finite elements [37]. Cracking was modeled using the smeared crack approach and reinforcement with embedded truss elements. The idealization assumptions of this study were also necessitated by the restrictions of the overwhelming computational demands of full-scale 3D finite element modeling.

Tang and Hao [33] investigated the mechanical behavior of reinforced concrete subjected to blast loads. Specific structural elements of a cable-stayed bridge were modeled with detailed 3D models. The overall response of the bridge as a result of losses in the capacities of these elements was monitored. Simulations run on LS-DYNA [38] revealed that computational demands were excessive even for numerical analysis of a single pier. It is worth noting that bond-slip behavior at the interface between concrete and steel reinforcement was regarded as a characteristic of concrete failure. This particular assumption is widely accepted and used (e.g. [24], [26], [32], [39]). Hence, it will also be adopted in the numerical analysis of this research work.

Bi and Hao [32] used LS-DYNA to construct a full-scale 3D model of a two-span RC bridge with a straight deck spanning 60 m to study the pounding damage due to spatially varying ground motions. The RC bridge consists of eight unreinforced elastomeric bearing pads modeled with 16 solid finite elements. Solid concrete elements with embedded rebars were assigned in the pounding regions. In contrast, smeared models (in which reinforcement is assumed to be equally distributed over the concrete elements) were assigned away from the pounding regions. This idealization procedure was introduced to minimize the computational demands.

Various commercial software packages have been adopted in the state-of-the-art literature to assess the mechanical behavior of RC bridges through finite element modeling. e.g. ANSYS [40], ABAQUS [41], DIANA FEA [42], Strand7 [43], Drain 3DX [44], OpenSees [45], ADINA [46] and GT STRUDL [47]. These software packages incorporate capable material damage models for concrete. As asserted in the literature, detailed 3D finite element models of RC structures that utilize the smeared cracking approach and embedded reinforcement elements are extremely powerful. However, these approaches impose significant and often restrictive computational demands [48]–[54]. Thus, many of the existing commercial software packages are often hindered from reaching optimal utilization levels to their full capabilities. This is particularly restrictive when the NLFEA incorporates 3D solid brick continuum elements in full-scale modeling large structures such as bridges.

In this paper, the 3D detailed modeling of concrete is generally implemented using 8-noded hexahedral elements. In the applicable sections, it is pointed out the differences between implementing the 8-noded and 20-noded elements for comparison purposes. The elastomeric bearings are also modeled using 8-noded hexahedral elements. A parametric investigation is performed to investigate the adopted model's numerical response for simulating the isolation system's mechanical behavior. Additionally, explicit modeling of the post-tensioning system is developed and numerically investigated.

Finally, the bridge's seismic behavior is investigated upon complete construction of the detailed 3D model. Full-scale modeling of an RC bridge spanning 100 m, with an arc-shaped deck (due to a curve along the span, which can be seen in the elevation view of the bridge in Figure 5a), will be performed using ReConAn FEA (finite element analysis) research software [55]. For the latest numerical advancements in relation to Reconan FEA, one can refer to [75]-[76]. It is important to note here that Reconan FEA was extensively validated through numerous experimental data derived through monotonic and cyclic testing of RC specimens or full-scale structures, including soil-structure interaction [77][78].

This research work foresees to assess the preliminary design of the bridge through pushover analysis. Numerical results will be compared to a simplified model developed on SAP2000. As mentioned in the 3D detailed model adopted in this work, concrete elements are discretized with eight-node hexahedral elements. The elastomeric bearings are also modeled using eight-node hexahedral elements. Moreover, the reinforcement is discretized with embedded two-node rod elements, which are assumed to have perfect bonding with the concrete elements. The 3D geometry of the reinforcement grid is completed in accordance with preliminary technical drawings. A comprehensive structural assessment of the studied bridge's preliminary design was achieved utilizing modal pushover analysis.

2 RESEARCH SIGNIFICANCE

High-fidelity 3D modeling of RC structures using the smeared crack approach and embedded reinforcement elements is endorsed by many researchers as a highly accurate numerical approach. It is routinely used to investigate structural elements' mechanical behavior, including ultimate loading conditions. However, the sheer volume of encountered numerical nuisances throughout the nonlinear solution algorithms' execution is often overwhelming. These complexities arise for many reasons, such as crack initiation, development, propagation, reinforcement yielding, etc. This makes the smeared crack modeling approach computationally demanding and, in many cases, numerically unstable (i.e., the solution fails to converge). Moreover, discretizing a structure with solid finite elements generates additional computational demands, whereby the stiffness matrices are larger and thus demanding huge memory and storage allocations. As a result, this modeling approach does not lend itself to practical upscaling and extension to full-scale modeling of RC structures.

In this work, modal pushover NLFEA and displacement-controlled cyclic pseudostatic NLFEA are presented for a case of a full-scale 100 m RC bridge. The discretization is done using 8-noded hexahedral continuum finite elements. Concrete cracking is accounted for through the smeared crack approach in a numerically-efficient protocol. The isolation system of the considered bridge consists of eight elastomeric bearings (steel-reinforced natural rubber), which are also modeled using 8-noded hexahedral elements. Researchers used this modeling approach of elastomeric bearings to independently investigate the bearings' mechanical behavior under different loading conditions. i.e., the simulation is carried out for a single elastomeric bearing without attachments to other structural elements. The elastomeric bearings are incorporated into the RC bridge mesh, maximizing the accuracy of the structural elements' overall mechanical behavior. As applied with the steel rebars, the prestressing cables of the bridge are also modeled as embedded rebar elements. The prestressing force is numerically incorporated through a novel algorithm as well. A parametric study was performed to verify the performance of the proposed algorithm. The computational efficiency and robustness of the proposed methodology will also be discussed. It is also important to note that extensive validation of the software used herein, ReConAn FEA, was performed using numerous experimental tests on RC structural members and full-scale structures. A comprehensive list of publications can be found in [56].

3 ELASTOMERIC BEARINGS

One of the objectives of the numerical study highlighted in this section is to determine the best configuration for modeling the elastomeric bearings and their maximum carrying capacity. In addition, a parametric study is run to investigate the mechanical behavior of the composite steel/rubber elastomeric bearings under compressive and shear loading. In a study by Newhouse et al. [40], [57], a detailed 3D analysis was performed to determine the deformation of hyper-elastic elastomeric bearings positioned at the location of lateral deflection using ANSYS. The numerical results of the study aligned closely with experimental results, concluding that analysis based on the use of solid finite elements is an effective research tool.

The bridge structure considered in this study is a two-span bridge with eight bearings included as supports; three at the right and left abutments and two at the middle piers. A previous study on the detailed 3D modeling of standard reinforced elastomeric bearings is available in [58]. For simplified modeling on

SAP2000, the reinforced elastomeric bearings were modeled with two-joint links. The compressive, shear and rotational stiffness coefficients (K_C, K_S, $K_{\theta X}$, $K_{\theta Y}$, $K_{\theta Z}$) of the standard reinforced elastomeric bearings were computed in accordance with [59] (See Eq. 1-7). The material properties summarized in Table 1, proposed by [60], were used as input parameters for the stiffness calculations.

$$K_C = \frac{EA}{t_{rl}} \tag{1}$$

$$K_S = \frac{GA}{t_{rl}} \tag{2}$$

$$K_{\theta i} = \frac{EI_i}{t_{rl}}, i = X, Y \; and \; Z \; axis \tag{3}$$

$$E = E_b + \left[\frac{C_1 G S^2}{1 + \frac{C_1 G S^2}{0.75\,B}}\right] \tag{4}$$

$$E_b = 4G\left[1 - \left(\frac{q}{1+q^2}\right)^2\right] \tag{5}$$

$$q = {}^{L}/_{W}, L \; and \; W: length \; and \; width \; of \; the \; bearing \; (W \leq L) \tag{6}$$

$$C_1 = 4 + q(6 - 3.3q) \tag{7}$$

Where:
E is the effective Young's modulus,
A is the gross area of the elastomeric bearing,
t_{rl} is the total thickness of the elastomeric material,
G is the shear modulus (assumed 1 MPa [2]),
I_i is the second moment of inertia about axis i,
q is the aspect ratio of bearing cross-sectional area,
C_1 is a constant related to the shape of the bearing,
S is the bearing shape factor,
E_b is the homogenous Young's modulus of the bearing,
B is the bulk modulus (assumed 2 GPa [59]).

Table 1: Elastomeric Material properties

Young Modulus E (GPa)	Ultimate Stress f_u (MPa)	Poisson Ratio ν
3,5 x 10^{-3}	30	0.49

The numerical results derived after implementing the above equations for the middle elastomeric bearings can be seen in Figure 1a (the formulas were programmed in MATLAB).

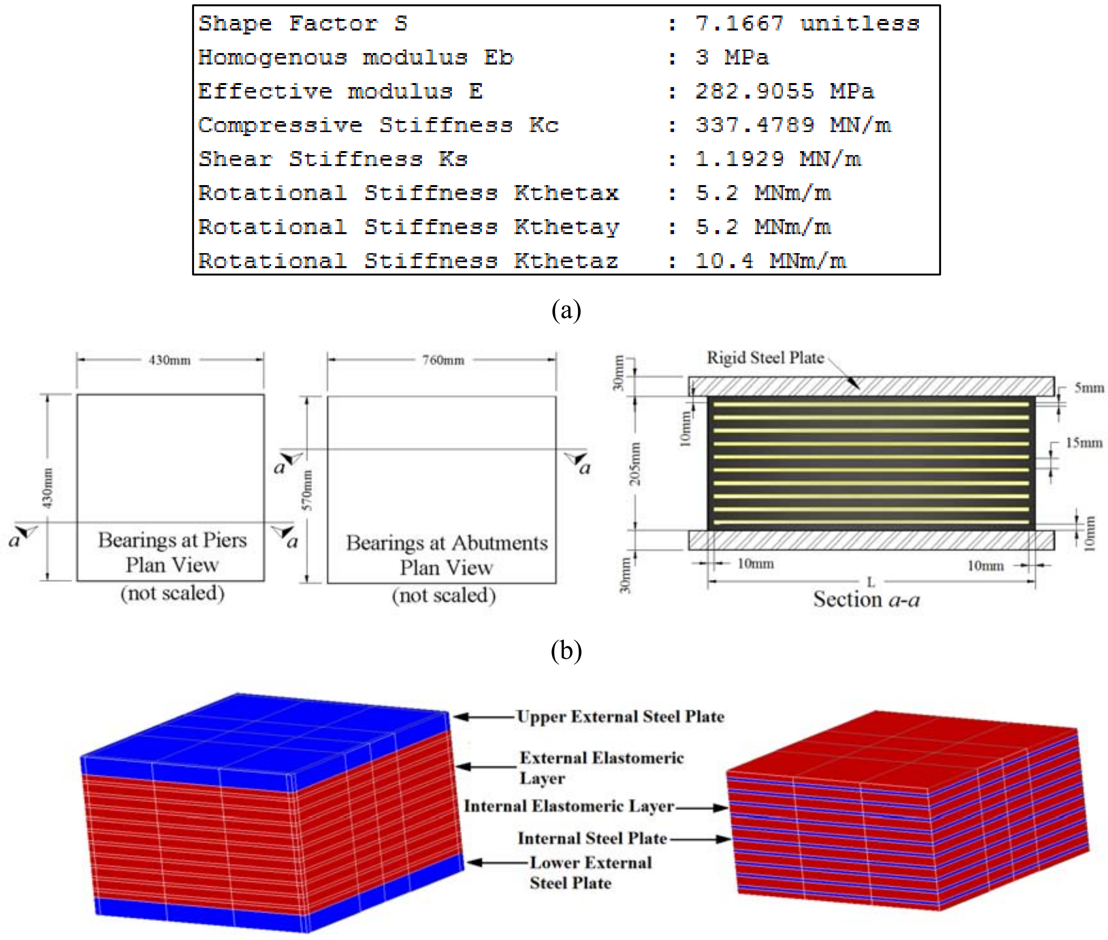
```
Shape Factor S                  : 7.1667 unitless
Homogenous modulus Eb           : 3 MPa
Effective modulus E             : 282.9055 MPa
Compressive Stiffness Kc        : 337.4789 MN/m
Shear Stiffness Ks              : 1.1929 MN/m
Rotational Stiffness Kthetax    : 5.2 MNm/m
Rotational Stiffness Kthetay    : 5.2 MNm/m
Rotational Stiffness Kthetaz    : 10.4 MNm/m
```

(a)

(b)

(c)

Figure 1: (a) Numerical data (for middle bearings), (b) Internal layer geometrical features and their plan views, and (c) Detailed FE meshing of elastomeric bearing.

In order to assess the mechanical behavior of the RC bridge preliminary design, the elastomeric bearings were modeled separately through 3D detailed numerical models to determine their maximum carrying capacity (see Figures 1b and 1c). In this work, a typical von Mises material model is used to simulate the mechanical behavior of the elastomer and steel plates to avoid complications introduced by material complexity and computational demands. A numerical investigation was run to derive an appropriate Young's modulus for the material to obtain realistic deformations of the elastomer in response to the applied load. Upon performing this investigation by comparing the link elements (springs with stiffnesses equal to those given in Figure 1a) to the proposed 3D detailed model (see Figures 1b and 1c), it was found that an elastomer Young's modulus of 12 MPa yielded the highest agreement. Moreover, it is widely recognized that under static loading, except for tensile regions near the external elastomeric layers, the strain field within the volume of the elastomeric bearing is mainly compressive [57]. Thus, the assumptions above will not significantly affect the results since tensile failure is not expected, so the tensile force does not influence the results under static loads.

In addition to calibrating the elastomer Young's modulus, several analyses were performed to study the numerical response of the middle bearings of the model in greater depth. These analyses fall into two main categories. The first category assumes that the load applied on the top steel plate of the bearing is a vertical load of 600 tons (to derive the ultimate carrying load (V_u)). In comparison, the second category assumes four different displacement levels, which are percentages of the ultimate vertical load (V_u); 18.5% (100 tons), 29.6% (160 tons), 37% (200 tons), and 50% (270 tons), as well as a horizontal load of $H_u = 20$ tons. Since it is challenging to estimate expected displacements, percentages of vertical load were used, and numerical results of either displacement or force are similar in the ascending branches, which applies to this study. For comparison purposes, all the investigated elastomeric bearings were discretized using 8-node (Hexa8) and 20-node (Hexa20) hexahedral elements (see mesh for middle bearing in Figure 2a).

As discussed in [78], the 8-noded isoparametric hexahedral element has 24 degrees of freedom (DOFs), whereas the 20-noded isoparametric hexahedral element foresees 60 DOFs. Therefore, the Hexa8 element is computationally efficient, whereas the Hexa20 is more accurate but more computationally demanding. The energy-based convergence criterion [78] was set to 10^{-5} for all analyses presented in this research work.

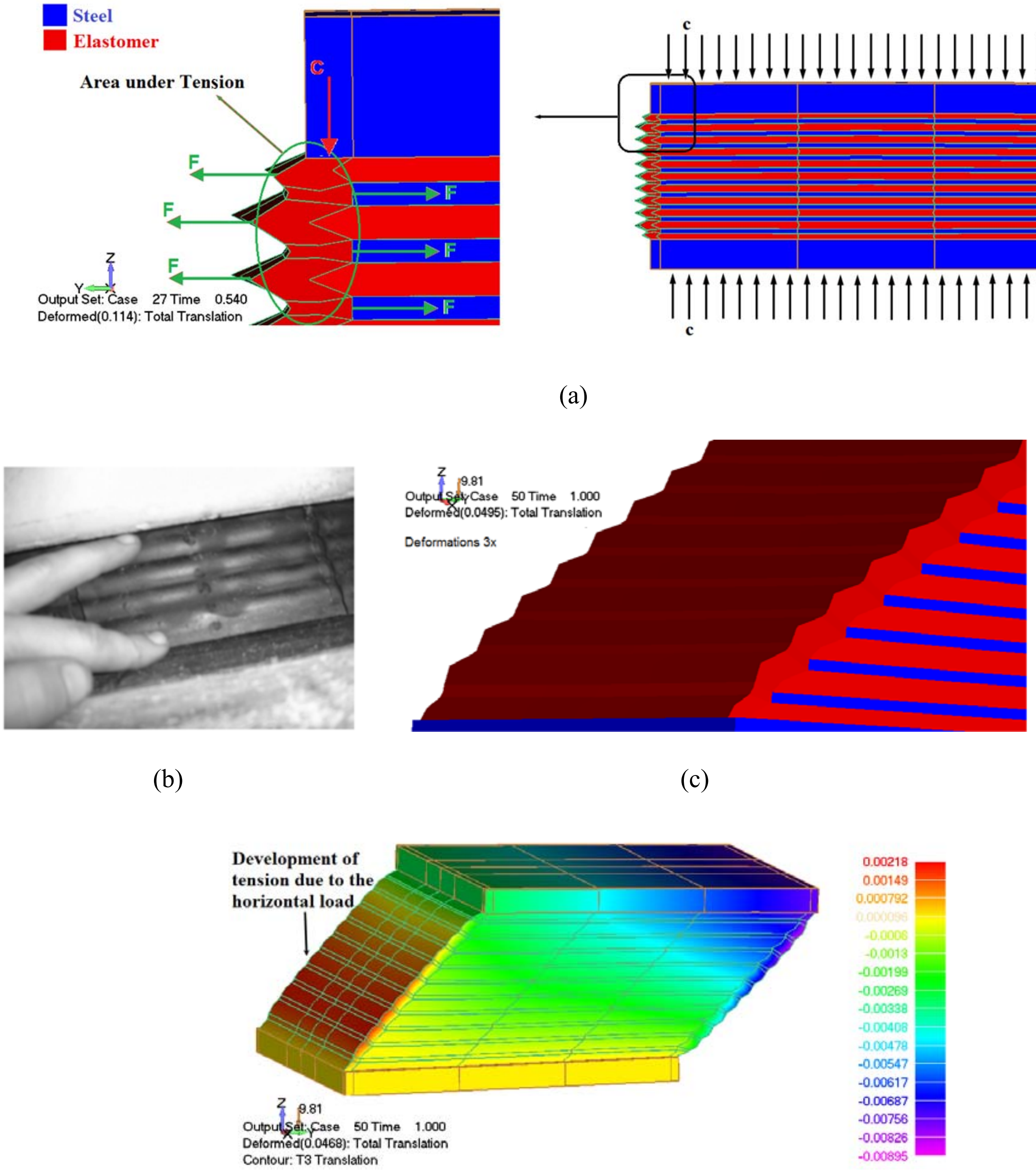

(a)

(b)

(c)

(d)

Figure 2: Deformed shape of (a) Hexa20 model for V = 540 tons (or 5.4MN); (b) Reinforced elastomeric bearing with steel plates after tension debonding [57]; (c) Resulted bearing from the Hexa20 model (50% V_u + 100% H_u) and (d) Elastomeric bearing due to load combination 1 (Hexa20 FE model – Load Combination 1) along with its translation contour on the z-axis

Figure 2a demonstrates the deformed shape of the Hexa20 FE mesh, for which the vertical deformation corresponding to a vertical load of 540 tons was found to be 30.4 mm. This value is 22.3% larger than the deformation (24.8 mm) obtained using Hexa8 finite elements. This may be attributed to the more flexible numerical formulation of the Hexa20 FE model. Therefore, the final model consisted of 8 noded elastomeric bearings. The elastomer expands horizontally due to excessive compression induced by the vertical load applied to the external steel plate. At the same time, the intermediate laminated steel plates constrain lateral expansion, and thus rubber bulges out. As illustrated in Figure 2a, the external layers of elastomer material bulge laterally due to compression; thus, a folded-like deformation develops due to the steel plate reinforcement. A similar type of folding is observed in Figures 2b and 2c, in which a physical bearing specimen was experimentally tested by Newhouse et al. [57], and the loading type was a combination of compressive and horizontal loads.

Table 2: Numerical results derived from the analysis when applying different load combinations.

Load Combination	Linear Vertical Dead Load V in tons ($\%V_u$)	Max. Vertical Displ. at the first load step (mm)		*H* Load for which zz-tension occurs at the elastomeric layer at the base (tons)		Maximum Horizontal Displ. for *H = 20 tons* (mm)		Max. horizontal deformation of the elastomeric layer at the base (mm)	
		Hexa8	Hexa20	Hexa8	Hexa20	Hexa8	Hexa20	Hexa8	Hexa20
1	100 (18.5)	4.87	5.71	28	44	45.6	46.8	0.15	0.22
2	160 (29.6)	7.76	9.11	44	68	46.1	47.6	0.1	0.16
3	200 (37.0)	9.70	11.4	56	84	46.6	48.2	0.07	0.13
4	270 (50.0)	13.1	15.3	72	112	47.5	49.5	0.04	0.08

Upon completion of the first set of analyses, the second set of numerical results was obtained by applying different levels of vertical loads (representing gravity loads applied at the first load increment) and a horizontal load of 20 tons, which was applied incrementally at the top external steel plate. The numerical results are summarized in Table 2. Figure 2d illustrates the deformed shape and z-displacement contour of the Hexa20 model for the first load combination. The tension strains develop at the external elastomeric layer and the lower bearing area (i.e., 1st elastomeric layer at the base and the bottom steel plate), which eventually tends to lift up the bearing. Therefore, the larger the vertical load applied, the smaller the vertical upward lift due to the horizontal loading.

For the case of the two middle bearings connecting the piers to the deck of the understudy RC bridge, a 30 MPa ultimate stress resulted in a maximum carrying capacity of 555 tons. This result is larger than the 300 tons anticipated by the manufacturer VSL [61], which was predicted for a similar elastomeric bearing (400x500 mm). According to the VSL specifications, applying a load of 300 tons induces a stress of 15 MPa in the bearings. To achieve the ultimate stress of 300 kg/cm^2 (30 MPa), a vertical load of approximately 600 tons was required, double the load the manufacturer predicted. The numerical model can be expected to fail when the rubber material develops its maximum stress. At this point, the elastomeric bearing will not be able to carry additional loads.

4 PRESTRESS MODELING

It is a common practice to simulate pre-tensioning and post-tensioning as a temperature change or as a set of axial and distributed loads on the structural member under compression [47]. For the sake of this research, ReConAn was equipped with the necessary numerical tools to account for pre-tensioning and post-tensioning forces applied directly to the cables, which were modeled as embedded rebar elements.

The algorithm developed to account for the compression induced in the concrete hexahedral elements at the material level entails the calculation of the initial stress and strain (σ_{i0} and ε_{i0}) in the embedded post-tensioned cable through Eq. 8. The internal force of the embedded cable ($\boldsymbol{F}_{R,Int.}$) is transformed through the kinematic expression given in Eq. 9 into a hexahedral internal force matrix ($\boldsymbol{F}_{H,Int.}$), which is defined as the initial force condition of the hexahedral element. Then, the internal force matrix of the hexahedral element, which incorporates the corresponding embedded cable element, is converted into an external load matrix ($\boldsymbol{F}_{H,Ext.}$) using Eq. 10. The external load matrix is then applied to the corresponding hexahedral nodes.

The first loading increment uses a numerical simulation of the post-tensioning effect, at which the numerical model's initial stress state is computed. Following the first loading increment, nonlinear load steps are applied incrementally until complete failure, and the new stresses and strains are updated according to Eq. 11.

$$\sigma_{i0} = \frac{F_P}{A_i}, \qquad \varepsilon_{i0} = \frac{\sigma_{i0}}{E_S} \tag{8}$$

$$\underbrace{\boldsymbol{F}_{H,Int.}}_{(24x1)} = \underbrace{\boldsymbol{T}}_{(24x6)} \cdot \underbrace{\boldsymbol{L}}_{(6x2)} \cdot \underbrace{\boldsymbol{F}_{R,Int.}}_{(2x1)} \tag{9}$$

$$\underbrace{\boldsymbol{F}_{H,Ext.}}_{(24x1)} = - \underbrace{\boldsymbol{F}_{H,Int.}}_{(24x1)} \tag{10}$$

$$\sigma_{i+1} = \sigma_{i0} + \Delta\, \sigma_{i+1}, \qquad \varepsilon_{i+1} = \varepsilon_{i0} + \Delta\, \varepsilon_{i+1} \tag{11}$$

A parametric study was run to verify the performance of the algorithm proposed to model the post-tensioning system. Figure 3a demonstrates the two FE models used to investigate the proposed algorithm. The two RC beams include two different cable geometries through which the post-tensioning force is applied. Both models employ two cables with a diameter of 28 mm each. The first model assumes a straight cable at a distance of 63 mm from the lower edge of the beam, while the second model assumes a curved cable profile. The total post-tensioning force was 100 kN per cable, which was determined appropriately to avoid any concrete cracking. The beams were initially assumed to be weightless to investigate their mechanical behavior in response to the post-tensioning cables. The cables' yielding stress was equal to 555 MPa, and thus the post-tensioning force of 100 kN is only 30% of the yielding force. The concrete's uniaxial compressive strength was assumed to be 22.5 MPa. These assumptions were made as per the reported results of Bresler and Scordelis [62], who tested a similar beam without prestressing it.

The maximum displacements obtained from the two models were 0.483 mm and 0.450 mm, respectively. Figure 3b illustrates the deformed shapes of the two models and the respective axial stress contours along the longitudinal axis of the beam. As illustrated, both models exhibit the same contour levels. It is noted that the post-tension cable generates a compressive stress field at the lower level of the beam in both cases, whereas tension is developed at the top cord of the two beams. It is also noted that the top cord of the curved-profile model is under partial tension (60% of the top cord) and partial compression (along the longitudinal axis of the beam). This is attributed to the curved geometry of the cable. i.e., the two ends of the cable are located above the centroid of the end sections at the supports (see Figure 3a). Figure 3c provides the deformed shape of the second model (curved profile model) when the self-weight of the beam is accounted for. The figure shows that the stresses decreased at the mid-section while the stresses at the supports increased. This is due to the combination of self-weight and the prestress. The shape of the beam flattens (as shown in Figure 3c) due to the increased loading (self-weight) on the beam surface, which pushes the beam downwards.

The curved profile was utilized due to its obvious load-deflection advantages. An ultimate limit state analysis was performed by applying a uniform distributed load on the top cord of the beam's section. Figure 4a shows the produced P-δ curve. As illustrated, the beam develops a negative displacement (upward displacement due to post-tensioning) until the total vertical load reaches 80 kN. The P-δ curve shows that cracking occurs at a total load of 213.2 kN, and then the beam fails at a total load of 754.5 kN, with a maximum deflection of 15.2 mm. The same RC beam was analyzed without any post-tensioning (see P-δ curve in Figure 4a), maintaining the same geometry and reinforcement level, to identify changes in the mechanical behavior due to prestressing. Without post-tensioning, cracks developed at the first loading increment, and the beam failed at a smaller load (18% smaller). Figure 4b shows the deformed shapes and the cracking patterns of the post-tensioned beam at critical load levels.

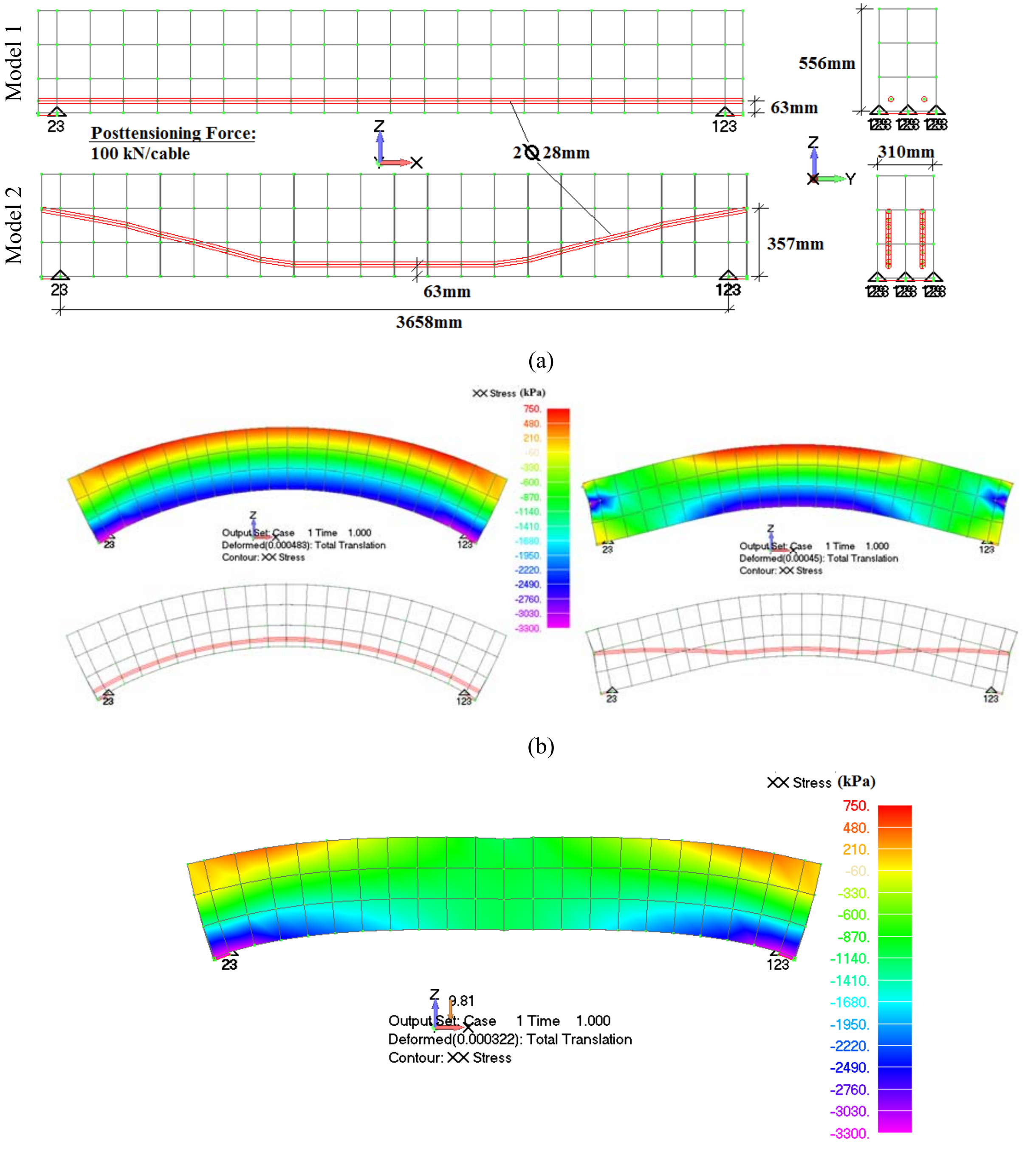

(a)

(b)

(c)

Figure 3: (a) RC beam models with straight and curved post-tensioning cables, (b) Axial stress contour and deformed shape of the two models (excluding self-weight), and (c) Axial stress contour and deformed shape of the FE model with the curved cable (including self-weight)

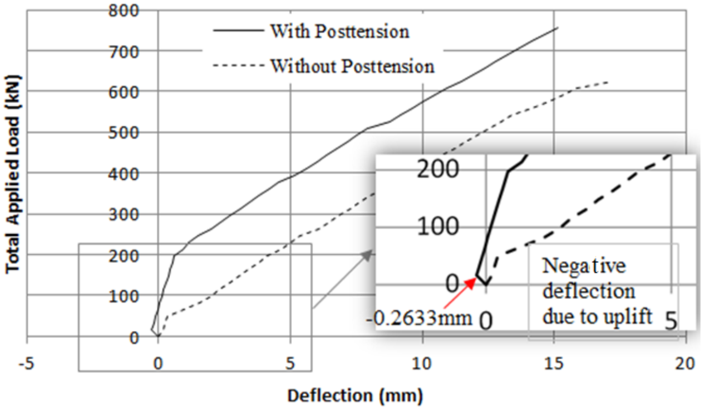

(a)

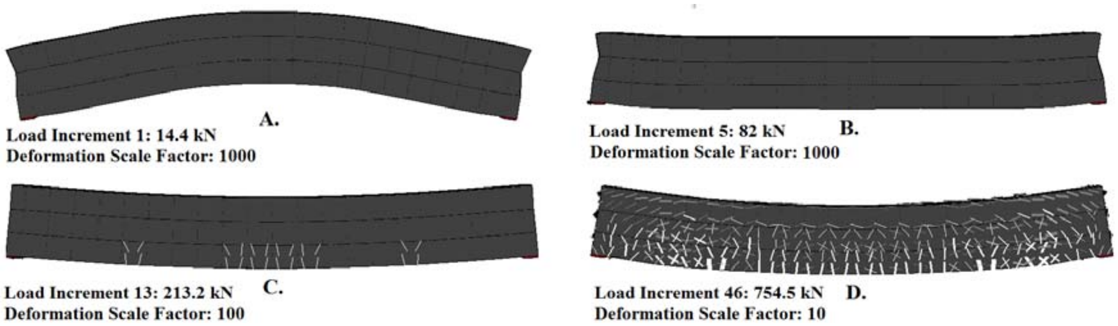

(b)

Figure 4: (a) P-δ curve and (b) Deformed shapes and crack patterns for the case of the second model (curved cable with post-tension).

5 GEOMETRY AND MODELING OF THE BRIDGE

The bridge has an effective span of 99.1 m, of which 51.55 m is the left span and 47.55 m is the right span [63]. The total height of the two piers is 5.6 m, with a spacing of 5 m. The bridge's trapezoidal deck is assumed to have a total width of 10.38 m and a height of 2.3 m. Figure 5 illustrates the elevation view and the geometric properties of the bridge's piers and deck, respectively. Reinforcement details and further details of the bridge's geometry are available in the literature [63].

The RC bridge understudy was discretized with hexahedral elements, as illustrated in Figure 6a. A convergence analysis was performed for different structural parts of the bridge to verify the finite element mesh. The average size of the hexahedral mesh element was 20 cm. Moreover, the selected hexahedral element size was optimal when using the Kotsovos and Pavlovic material model [49], which was adopted in this work.

Furthermore, the Menegotto-Pinto material model was adopted for the embedded steel rebars, illustrated in Figure 6b. The total number of concrete hexahedral elements used in the FE mesh was 102,622, and the total number of embedded rebar macro-elements was 47,839. Figure 6c illustrates the detailed FE mesh and the 3D model geometry of the connection between the deck and the two piers.

A total of eight bearings were included; three at the right and left abutments and two at the piers. The FE mesh incorporates a detailed bearings model comprising 5,520 hexahedral elements, unlike the 312 elements in a previous simulation model [63].

A summary of the RC bridge mesh and the embedded rebar elements is provided in Table 3. Upon completion of the mesh generation, the total number of embedded rebar elements was 520,624, and the required computational time for mesh generation was approximately 43 minutes [63]. The methodology adopted for the embedded rebar mesh generation was proposed by Markou and Papadrakakis [54], which is an extension of Markou's work [64].

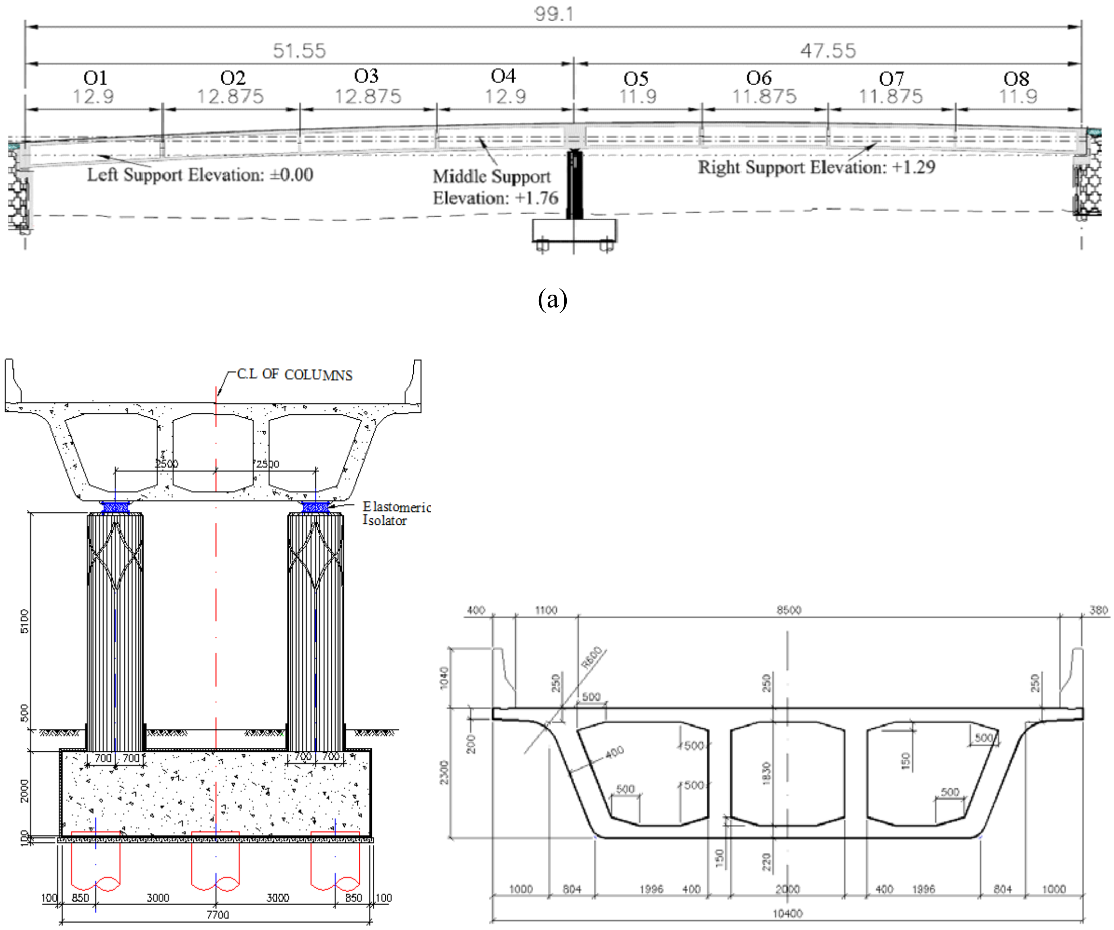

(a)

(b)

(c)

Figure 5: (a) Elevation view, (b) Pier geometry, and (c) Trapezoidal deck geometry of the bridge (in mm)

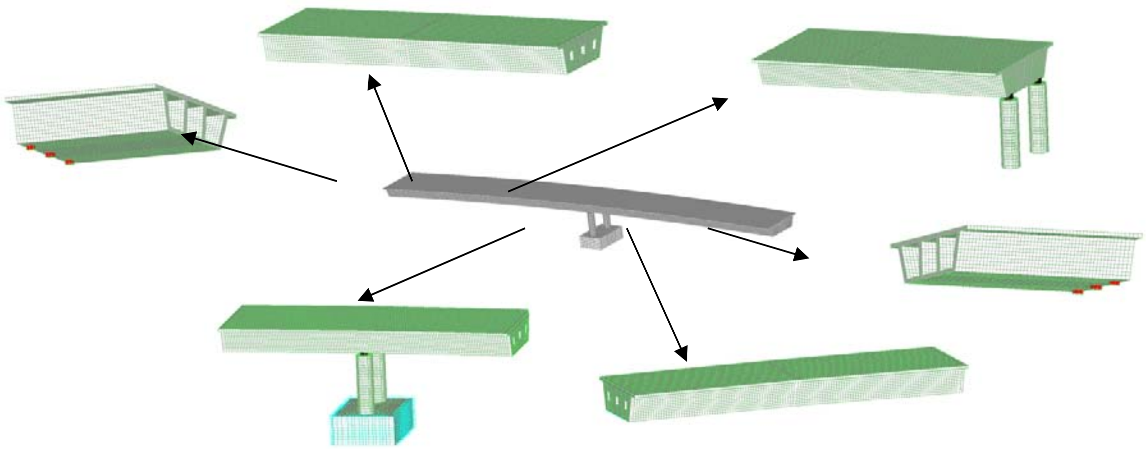

(a)

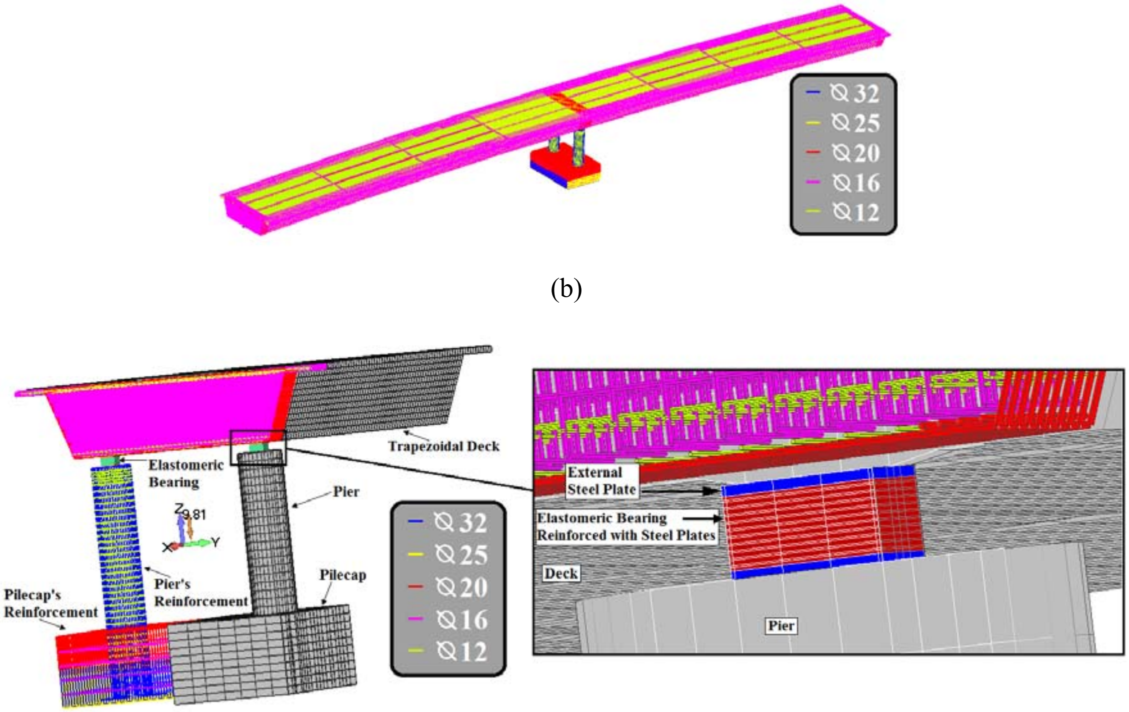

(b)

(c)

Figure 6: (a) Mesh convergence analysis procedure, (b) Macro-element rebar mesh, and (c) Detailed FE mesh of the bridge.

As illustrated in Figure 6a, the RC bridge mesh comprises the discretization of the deck, the two piers, and the pile cap. Given that the pile cap is assumed to be fixed at the base. The standard reinforced elastomeric bearings at either abutment are also fixed at their bases. The piling system and the left and right abutments were excluded from the study as they introduce issues beyond the scope of this research work (expansion joints, pounding effects, bridge/backfill interaction effects, soil-structure interaction effects, etc.).

Due to the unavailability of information on the material properties, concrete is assumed to be material C90, and steel reinforcement is assumed to be material S500. Given that the bridge was constructed in the UAE, the assumption of using high-strength concrete aligns with common practices. The material properties adopted in the numerical models are provided in Table 4.

Table 3: Summary of RC bridge mesh and embedded rebar elements

a/a	Description	Value
1	Number of Hexahedral Concrete Elements	102,622
2	Number of Hexahedral Elements (Bearings)	5,520
2	Number of Nodes (hexa8 only)	175,784
3	Number of Macro-Elements	47,839
4	Total Number of Embedded Rebar FEs Generated	520,624
5	Total Number of Short Embedded Rebar FEs that were Discarded by the Filter Algorithm (refer to [54], [63], [64] for further details on the Filter algorithm)	1,439
6	Required Embedded Mesh Generation Time	42 m 22 s

Table 4: Material properties

a/a	Material	Unit Weight, γ (kN/m^3)	Young Modulus, E (GPa)	Strain-Hardening Modulus, E_T (GPa)	Yield Stress, f_y (MPa)	Ultimate Strength, f_u (MPa)	Ultimate Strain, ε_u	Poisson Ratio, ν
1	Concrete	24	44	-	-	90	-	0.2
2	Reinforcement Steel	78	200	2	500	695	0.10	0.3
3	Steel Plates	78	200	2	400	595	0.10	0.3
4	Elastomeric material	-	3.5 x 10^{-3}	-	-	30	-	0.49
5	Prestressing tendons	78	210	2	1030	1030	0.15	0.3

Figure 7 illustrates the simplified FE mesh constructed on SAP2000, in which the deck is discretized with 11,792 shell elements while the piers were modeled as beam-column finite elements.

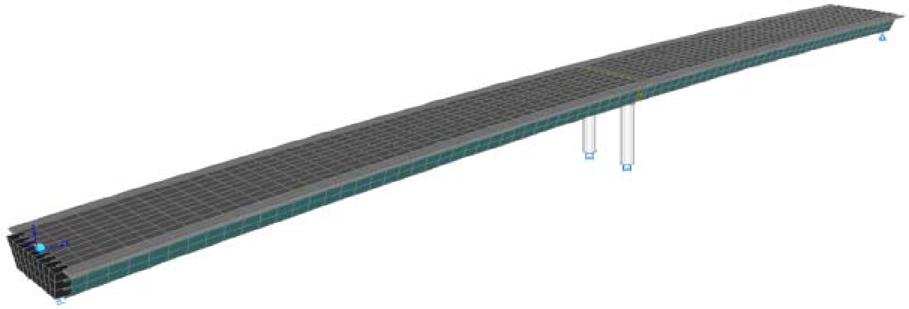

Figure 7: The simplified model constructed on SAP2000

6 LINEAR ELASTIC SOLUTION WITHOUT EMBEDDED REBARS

The next stage of assessing the numerical model and the overall mechanical behavior of the bridge understudy was to linearly analyze the complete hexahedral model (Hexa8) under just the structure's self-weight. The results of this analysis were compared with results from the simplified SAP2000 FE model (see Figure 8a), for which a mesh sensitivity analysis was performed to determine the optimal FE mesh size providing both reasonable accuracy and computational efficiency. Three FE sizes were tested; 130 cm, 70 cm, and 30 cm, respectively. It was found that discretizing the bridge using rectangular FE shells with an edge size of 70 cm satisfied the preceding criteria.

Figure 8b demonstrates the z-axis translation contour derived from the Hexa8 FE mesh. It is noted that the maximum deflection of the bridge occurs at the left span of the deck and is equal to 53.7 mm. A lesser maximum deflection (45.5 mm) was obtained from the simplified FE model, as illustrated in Figure 8a. It was also found that the compressive deformations due to the bearings at the piers were 21 mm and 26.5 mm, for the simplified and detailed models, respectively. Therefore, the difference in the maximum deflections is attributed to the deformation of the elastomeric bearings. One of the reasons that the bearing's displacement for the case of the Hexa8 model is greater than that of the simplified model is that ReConAn increases the nominal weight of concrete by a factor of 1.03 to account for the reinforcement's self-weight. Nonetheless, this was found to have a relatively small effect on the overall effect of RC structures.

As presented by the SAP2000 model, the resultant compressive force at the top surface of each pier due to the structure's self-weight was 5.83 MN. This compressive load exceeds the bearings' ultimate carrying capacity (5.55 MN) connecting the piers to the deck. Thus, redesigning is required, possibly by increasing the bearings area. Figure 9a shows the deformed shapes of the bearings in the middle and at the abutments obtained from the Hexa8 model. The longitudinal x-translation of the left abutment was found to be equal to 6.9 mm, as opposed to 3.1 mm obtained from the simplified model. This finding confirms that the material model selected for the elastomer yields more flexible numerical results than the link elements utilized in the simplified model.

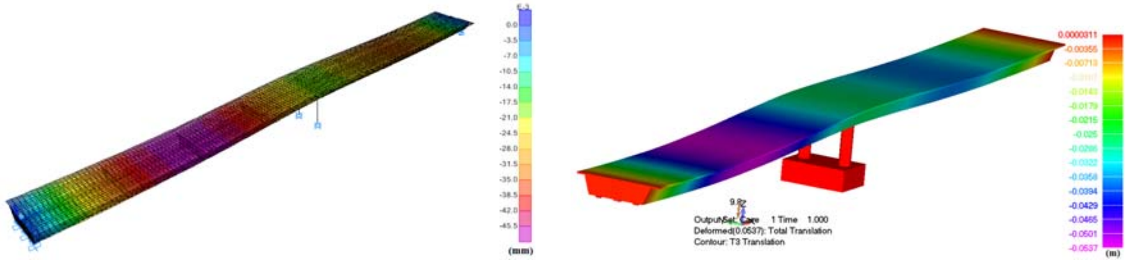

(a) (b)

Figure 8: Deformed shapes and translation contours along the z-axis of the RC bridge due to self-weight using (a) SAP2000 (Shell FEs) and (b) ReConAn (Hexa8 FEs)

It must be noted that the deflection differences observed in the deck's mechanical response would have been magnified if the shell FE meshes were constrained at the middle vertical diaphragm, which has a total diaphragm thickness of 2 m. Being constrained induces additional stiffness to the deck, thus, reducing the accuracy of capturing the actual stiffness contribution of the middle of the bridge. The same phenomenon applies in the case of 1 m thick vertical diaphragms located at the two ends of the bridge's trapezoidal deck.

Another key finding of this linear analysis is that stress concentrations developing at the contact areas between the elastomeric bearings and the deck are higher in the simplified model. This is attributed to using link elements to model the bearings in the simplified model. Link elements are connected to the deck at a single node, which explains the higher stress concentrations. Figure 9b shows the solid von Mises stress contours obtained from both models. The simplified model resulted in a von Mises stress at the connection between the bearing and the deck equal to 18.1 MPa, whereas the 3D model resulted in a von Mises stress of 14.7 MPa. The deformed shapes of the bearings are illustrated in Figure 9a, where the solid von Mises strain contour is also visualized.

The following assessment stage determines whether the RC bridge develops any cracks due to its self-weight, thus requiring a pre-tension system. The maximum deflection obtained from the linear analysis implies that the deck behaves relatively flexibly, given that no pre-tension was assumed.

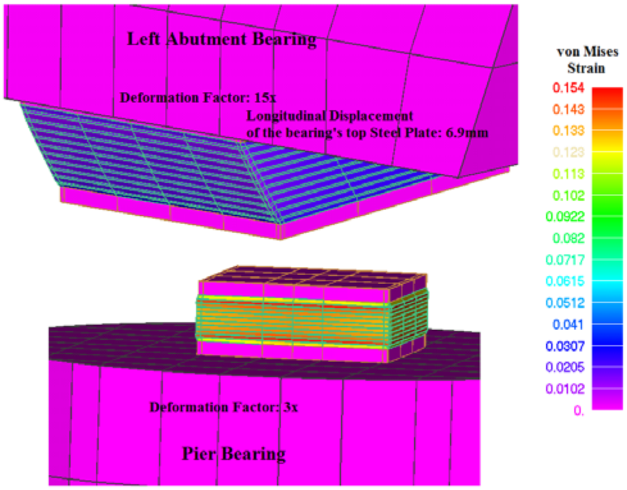

(a)

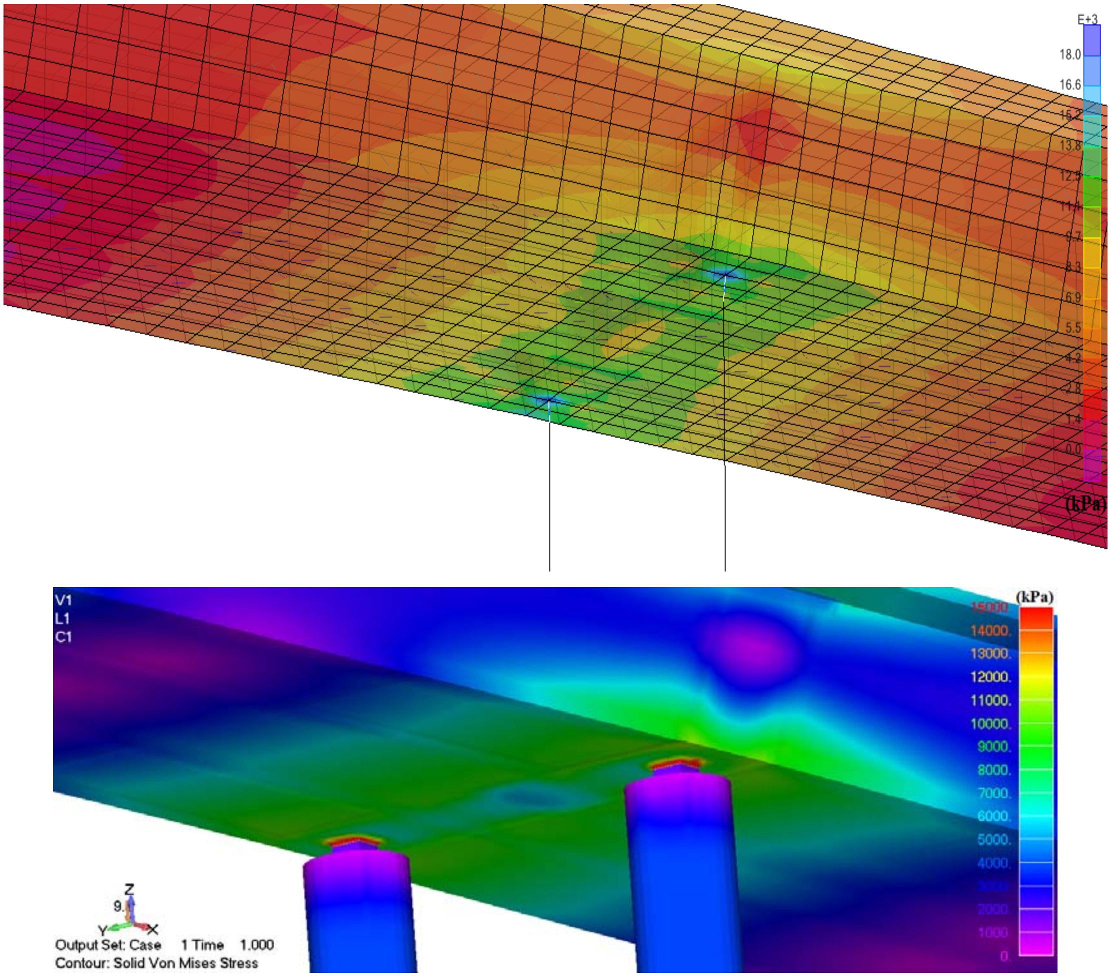

(b)

Figure 9: Von Mises strain contours of the (a) middle and left abutment elastomeric bearings; (b) bridge using SAP2000 (up) and ReConAn FEA (down).

7 NONLINEAR SOLUTION OF THE COMPLETE 3D DETAILED MODEL

This section presents the results of the nonlinear numerical solution of the complete 3D detailed model with embedded rebars and no post-tensioning. The FE mesh illustrated in Figure 6c is used to simulate and investigate the mechanical behavior of the RC bridge under self-weight. This numerical analysis aims to investigate potential stress concentrations and cracks, which signal the shortcomings of the bridge's preliminary design. The adopted model does not accommodate any post-tensioning techniques; therefore, cracking is expected.

The analysis revealed that the RC bridge is incapable of carrying its self-weight without developing cracks. Therefore, even larger cracks would be expected to develop at service loads. Moreover, due to the relatively long spans of the bridge, the bottom-right area of the bridge deck developed horizontal cracks. This is attributed to the stress fields generated by the bending and shear forces at the connection areas between the vertical walls and the lower slab of the RC deck (see Figure 10c). On the bridge's left span, cracking was developed at the vertical diaphragm and in the middle of the vertical walls (refer to Figures 10a and 10b, respectively).

To provide a closer insight into the stress distribution obtained from the nonlinear analysis described above, Figure 11 depicts a cut section of the model at the pier's bearing. It demonstrates the von Mises stress contours at the pier's head due to the bridge's self-weight. The compressive loads due to the bridge's deck are also illustrated. It was found that the pier's bearings were under-designed, with the elastomeric exceeding 50% of its ultimate stress, thus requiring a larger plan view area.

The maximum recorded displacement of the bridge was 30.4 mm, occurring at the middle nodes of the left span of the bridge. Compared to the previous two models, the stiffer behavior observed in this model can be attributed to the reinforcement being modeled as embedded rebar elements. Thus, in this model, reinforcement increases the stiffness of the deck, which is evident from the decreased maximum deflection.

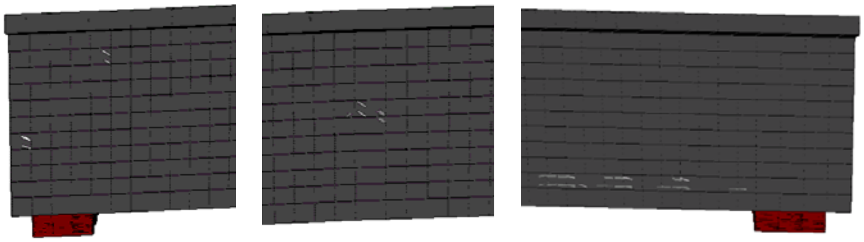
(a) (b) (c)

Figure 10: Crack patterns of the deck due to the self-weight load at the (a) left support, (b) middle of the left span, and (c) near the right support.

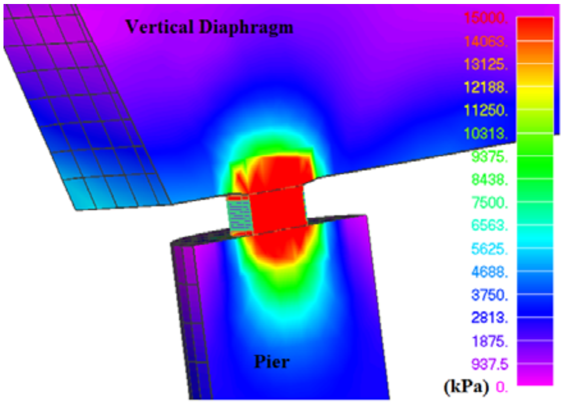

Figure 11: Von Mises stress contour at the connection between the pier and the deck (section).

8 REDESIGN WITH PRESTRESSING CABLES

The analyzed results discussed in the previous sections deemed the bridge's mechanical response unsatisfactory for two main reasons. Firstly, it develops large deflections, and secondly, it cracks under its own weight. The large deflections are attributed to the soft behavior of the pier bearings and the design of the deck's section. The elastomeric bearings at the piers were redesigned and resized to 70x70 cm to rectify these design flaws. In addition, a post-tensioning system was introduced to the bridge deck. Therefore, each vertical wall was reinforced with three post-tension cables, modeled as embedded reinforcement with prestressing attributes.

After the parametric investigation of the post-tensioning algorithm, the numerical model of the RC bridge was solved by neglecting the self-weight and any other gravitational loads to investigate the bridge's overall behavior due to the post-tension system. It is important to note that each cable element is assumed to have a circular section of 90 mm in diameter, while for this first full-scale post-tensioning analysis, the applied prestress force was equal to 250 kN (5% of the final applied prestress force). Figure 12b shows the SMAD Custom Properties software developed by Stavroulakis [65], through which the pre- or post-tension force is defined as a custom property. Moreover, the embedded mesh generation method allows for the inclusion of a substantial number of rebars inside hexahedral meshes, which is addressed in a recent study [66]. These innovative techniques are expected to transform the current state of the art in RC structural analysis and design [67]-[74].

Figure 13a shows the deformed shape of the RC bridge due to the prestressing force applied in the 12 post-tensioned cables, which were embedded in the four vertical walls of the RC deck. It can also be seen that the two spans move upwards while the middle elastomeric bearing is under compression due to the negative moment at the area connecting the deck to the piers (post-tensioned cables have a negative eccentricity, see Figure 12a). This numerical finding indicates that the post-tensioning system results in an additional vertical load transferred to the bearings connecting the piers with the deck. The same observation was made by applying the prestress in the simplified model in SAP2000 by assigning negative strain at the shell elements of the deck that incorporate the prestress cables. Figure 13a also shows that the left and the middle support have a downward movement due to the applied loads (excluding self-weight), while the right support has an upward movement. This is due to the higher post-tensioned force and resulting stiffness of the right span compared to the applied loads, which pushes the deck upwards. While for the left support, due to the longer span length, is less stiff than the right span, so it has a downward movement due to the applied loads.

Since this work aims to assess the bridge's seismic capacity, a detailed assessment of the post-tensioning system will not be elaborated. It is worth noting that the final model used for the pushover analysis assumes a prestressing force (P_p) of 300 kN per cable. Figure 13b shows the von Mises stress distribution of the bridge resulting from the analysis at service loads (i.e., self-weight of the bridge, self-weight of the asphalt layer, and live load). According to the analysis, the maximum deflection (including body translation) of the longest span of the deck was equal to 12.6 mm, and the maximum deflection relative to the supports was equal to 5.8 mm, while the corresponding compressive deformation of the elastomeric bearings at the piers was 8 mm (see Figure 13b).

The final step before pushover analysis was calculating the total quasi-static seismic load to be applied to the model. One of the most common methods used to perform nonlinear analysis under seismic loads is the Modal Pushover Analysis (MPA), adopted in this work [3]. The total seismic load was calculated according to EC8 [1] using the type I response spectrum. The assumptions made for calculating the design spectrum acceleration and total base shear are summarized in Table 5.

After performing modal analysis on SAP2000, it was found that the first two modes of the bridge under study are translational oscillations along the X and Y axes, respectively. Given that the model's Y axis is the lateral axis, the pushover analysis was performed by applying the horizontal seismic load on the deck's vertical wall along the Y global axis (2nd dominant mode seen in Figure 14).

Over ten loading increments, 15 MN was applied on the deck's vertical wall. The energy convergence criterion was set to 10^{-4}. Compared to the convergence criterion of 10^{-3} necessary for numerous internal iterations, the selected convergence criterion is considered to be relaxed. It is important to note here that when solving a hexahedral mesh with more than 100,000 elements, the numerical errors, such as rounding and other errors during nonlinear analysis, are quite significant. Thus, using a numerically unstable material model (material models in combination with the smeared crack approach), which imposes large unbalanced forces at each iteration, particularly during cracking, makes numerical convergence cumbersome. The corresponding derived energy convergence errors for the understudy model are shown in Figure 15. These errors were evaluated using the energy tolerance criterion.

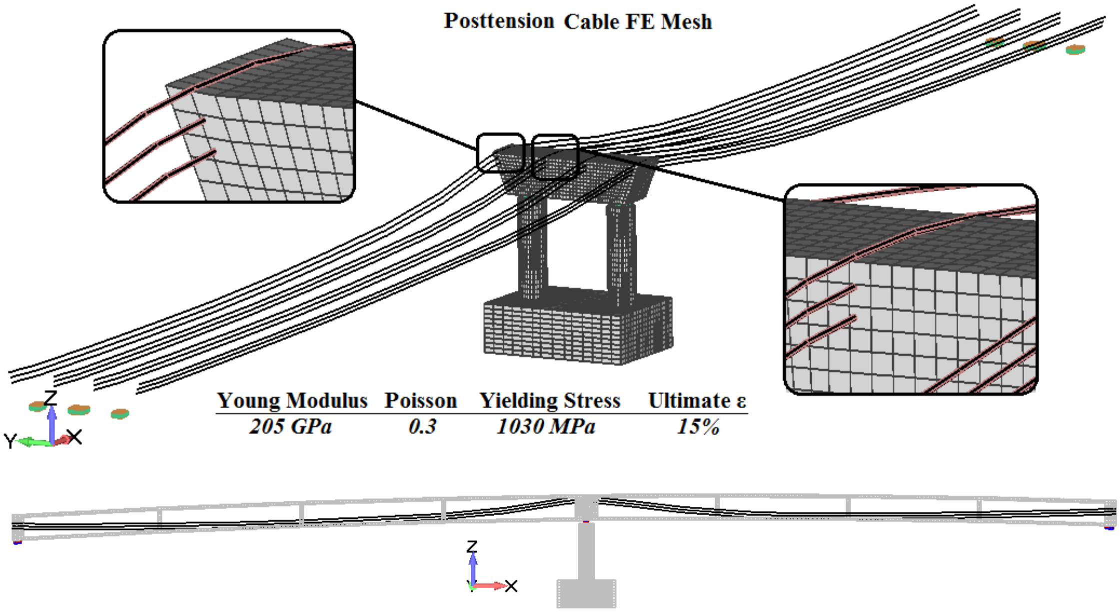

Young Modulus	Poisson	Yielding Stress	Ultimate ε
205 GPa	*0.3*	*1030 MPa*	*15%*

(a)

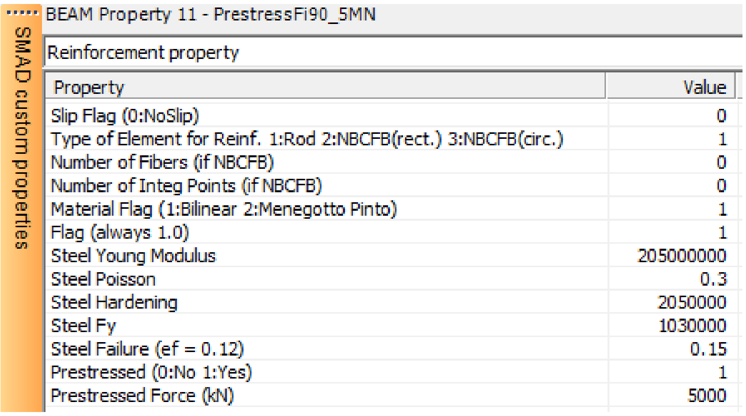

BEAM Property 11 - PrestressFi90_5MN

Reinforcement property

Property	Value
Slip Flag (0:NoSlip)	0
Type of Element for Reinf. 1:Rod 2:NBCFB(rect.) 3:NBCFB(circ.)	1
Number of Fibers (if NBCFB)	0
Number of Integ Points (if NBCFB)	0
Material Flag (1:Bilinear 2:Menegotto Pinto)	1
Flag (always 1.0)	1
Steel Young Modulus	205000000
Steel Poisson	0.3
Steel Hardening	2050000
Steel Fy	1030000
Steel Failure (ef = 0.12)	0.15
Prestressed (0:No 1:Yes)	1
Prestressed Force (kN)	5000

(b)

Figure 12: (a) FE mesh of post-tensioning cables and (b) Post-tensioning force definition for an embedded rebar property.

The numerical results from the nonlinear analysis showed that the deformed shape of the understudy bridge due to the horizontal load was similar to the second modal shape, while the elastomeric bearings were the structural members that developed the most significant deformations. As shown in Figure 16a, point β, located at a distance of 39 m from point α, exhibits the maximum horizontal displacement, while the deck behaves as a beam under bending. In addition to that, the left span (which is the longest one) transfers a greater load to its left support (point α), and this is the reason why the horizontal displacement of the deck at the left support is greater than that of the right support (point δ). Figure 16b shows the P-δ curves for the four monitored points (α, β, γ & δ), shown in Figure 16a, and the corresponding curves of the top nodes of the two piers. As can be observed from Figure 16b, the two piers do not exhibit the same horizontal displacement resulting in rotating the deck about the Z global axis (see Figure 16c); thus, the overall deformation of the bridge was asymmetric. It is important to note here that the energy convergence tolerance during the nonlinear analysis was set to 10^{-4}.

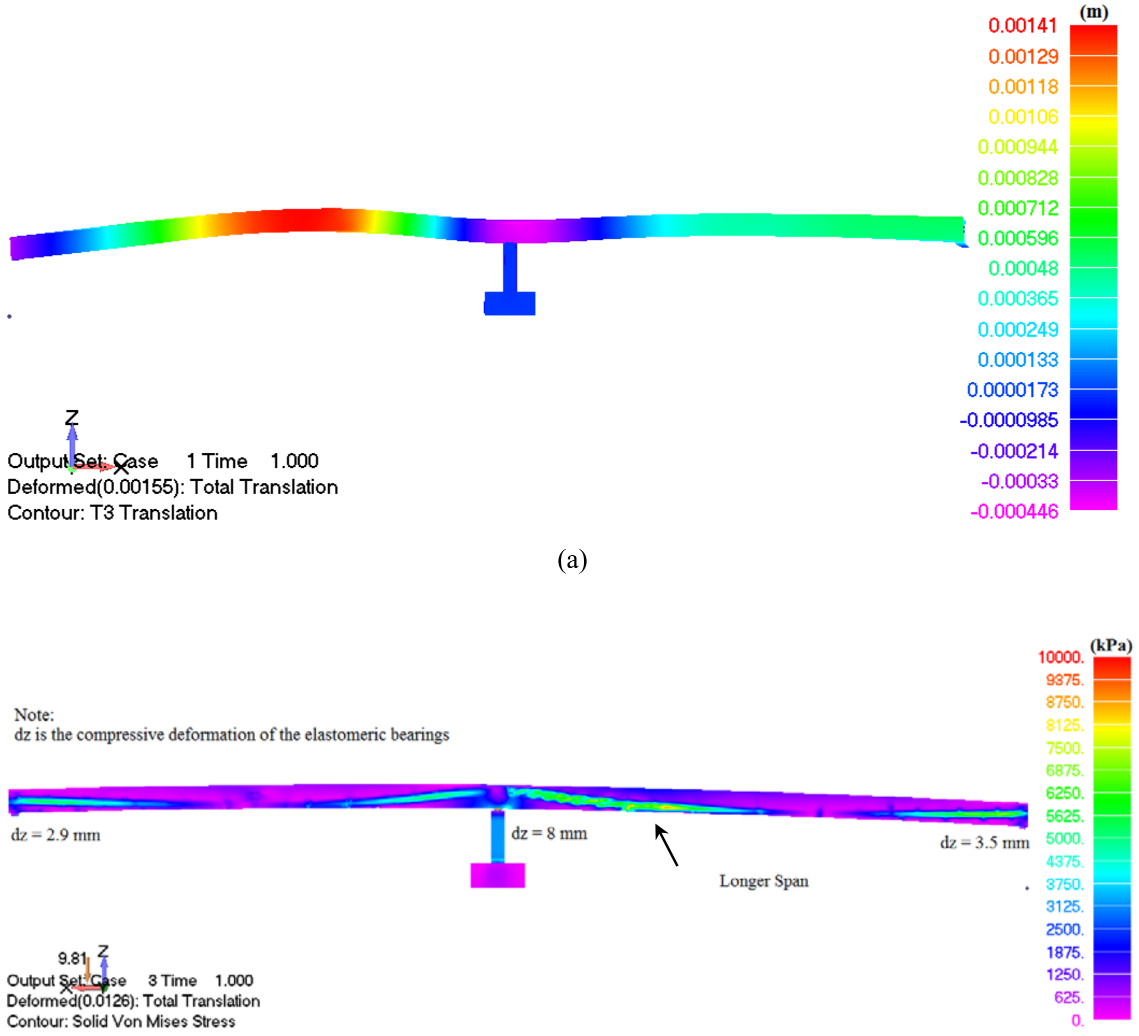

(a)

(b)

Figure 13: Deformed shape and von Mises stress distribution of the RC bridge due to post-tensioning (a) without self-weight and (b) with service loads.

Table 5: Seismic parameters assumed for the computation of the total base shear according to EC8.

a/a	Parameter	Value
1	Ground Type	B
2	Soil Factor S	1.2
3	Importance Factor γ	1.3
4	Acceleration a_g	0.2g
5	Behavior Factor q	1.0
6	Limit of the constant spectral acceleration branch T_C	0.5 seconds
7	Mode along the Y-axis T	1.36 seconds
8	Design Spectrum Acceleration, $S_d(T)$ =	0.191g
9	Total Base Shear V_S	7.66 MN

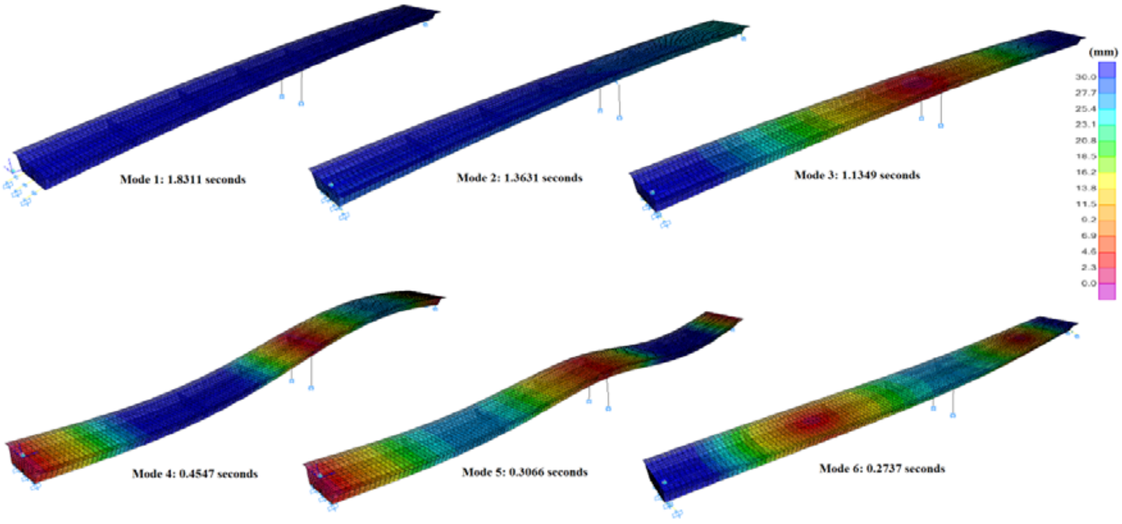

Figure 14: Mode shapes derived from SAP2000 (simplified model).

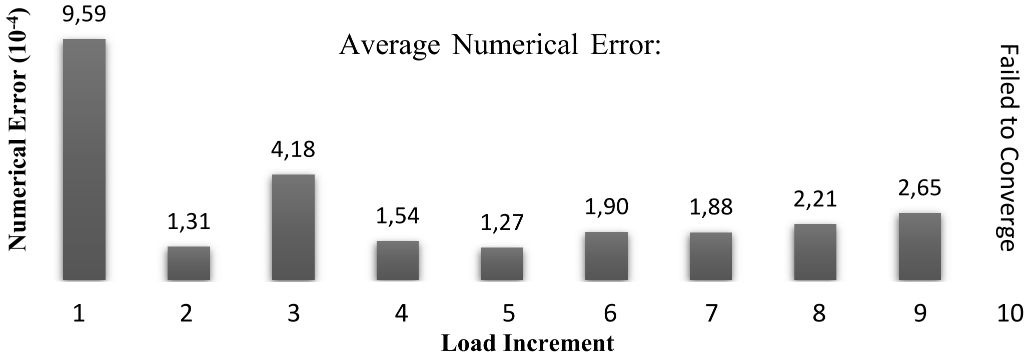

Figure 15: Numerical errors per load increment obtained from the nonlinear analysis.

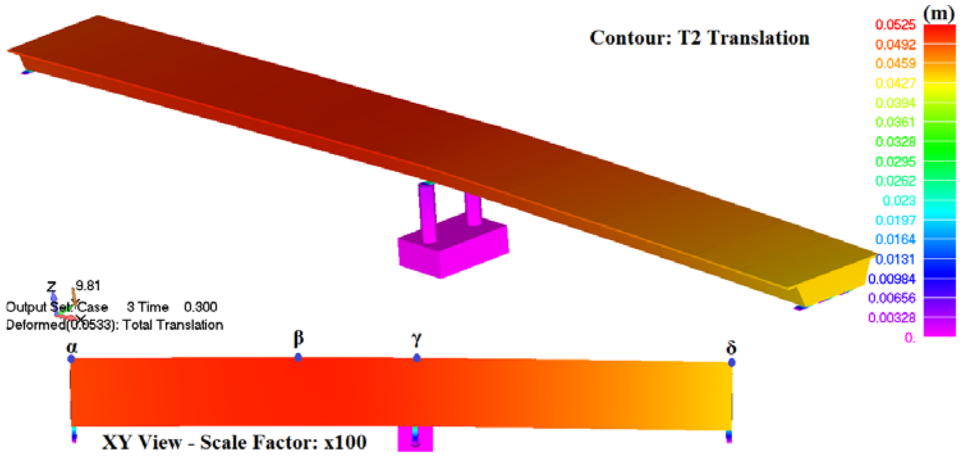

(a)

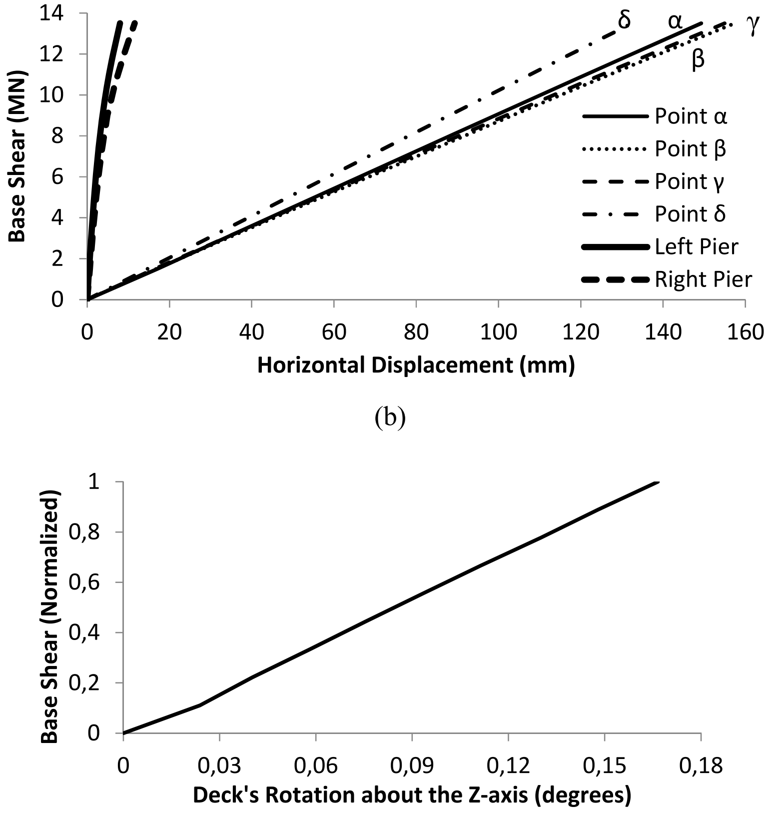

(b)

(c)

Figure 16: (a) Deformed shape at load increment 3 (Total applied horizontal load 4.5 MN), (b) P-δ curves, and (c) Deck's rotation due to horizontal loading.

The elastomeric bearing controls the failure mechanism, while the bridge deck does not develop any significant cracks prior to failure (V_{max} = 13.5 MN). The final model of the RC bridge accommodates the code's specifications for the base shear (7.66 MN), and the piers can resist the bending moments at their base. The maximum recorded horizontal displacement prior to failure was equal to 157.4 mm. This is attributed to the use of elastomeric bearings. They decouple the mechanical behavior of the pier from the deck, thus significantly affecting the bridge's stiffness. Decoupling of the mechanical behavior refers to the large horizontal deformation, which was recorded oblivious to the rebar failure due to the rigid body movements. It is also evident that the piers and deck do not deform significantly enough to achieve failure or yielding of the rebars.

Figures 17a and 17b demonstrate the crack patterns developing mainly in the base and head of the piers and the upper slab of the deck, which was under tension due to the deck's out-of-plane bending. Tensile cracks also developed in similar patterns at the lower slab of the deck, as illustrated in Figures 17a and 17c. The cracks at the base of the piers are attributed to the bending moments developed due to the horizontal loads transferred from the bearings to the piers. In contrast, the diagonal cracks at the pier heads are due to shear and torsional deformations. These observations reinforce the importance of providing adequate shear reinforcement to avoid potential structural vulnerabilities. Many designers increase the diameter of the pier head to increase shear resistance and prevent local cracking. For the investigated bridge herein, increasing the size of the pier heads is also suggested.

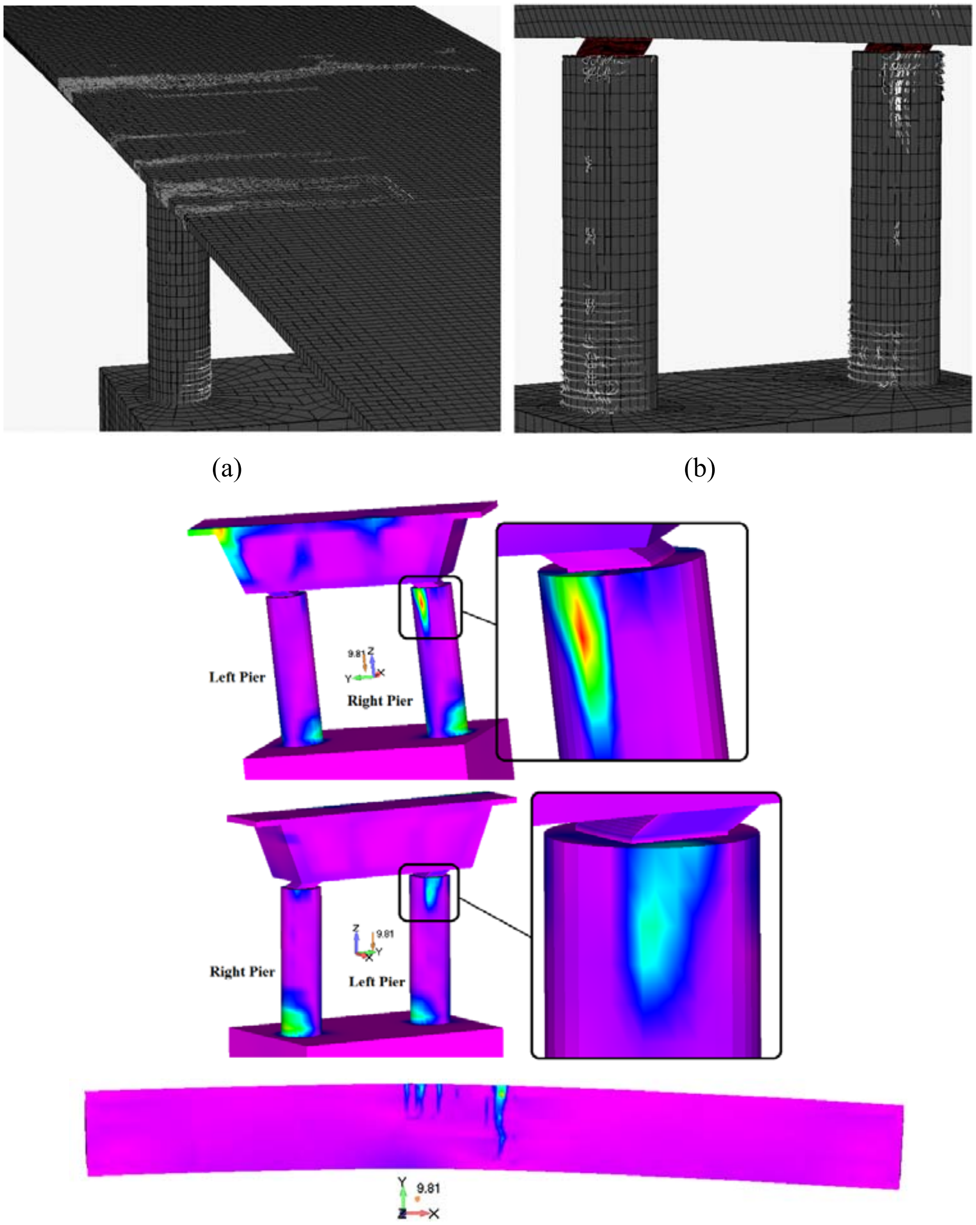

(a) (b)

(c)

Figure 17: Crack patterns developed prior to failure (a) on deck and (b) at bridge piers and (c) Von Mises strain contours of the (Up) piers and middle vertical diaphragm, and (Down) upper slab of the deck (seismic load direction: Y-axis).

The total computational time elapsed to complete all numerical procedures was 46 hours and 30 minutes. Mesh generation constituted 2.3% of the total computational time, while output data generation constituted 26.5%. As presented in Table 6, the nonlinear solution generates the highest computational demand, consuming 71% of the total computational time. This is mainly due to the stiffness inversion procedure, which includes a total of 798,697,535 matrix elements. It is also important to note that the 33 hours required for the nonlinear solution correspond to 100 internal iterations, each consuming 19 minutes and 48 seconds.

Table 6: General numerical details derived after the nonlinear analysis of the complete FE model.

a/a	Description	Value
1	Number of Hexahedral Elements	109,338
2	Number of Nodes (hexa8 only)	177,149
3	Number of Macro-Elements	49,172
4	Total Number of Embedded Rebar FEs Generated	529,332
5	Total Number of Short Embedded Rebar FEs that were Discarded by the Filter Algorithm (refer to [54], [63], [64] for further details on Filter Algorithm)	887
6	Required Embedded Mesh Generation Time	65 m 5 s
7	Required RAM for the Stiffness Matrix	5.95 Gb
8	Max Required RAM Allocated by the Software	20.65 Gb
9	Computational Time to Solve 10 Load Increments	33 hrs
10	Computational Time for Writing the Output Data	12 hrs 20m
11	Total Computational Time	46 hrs 30m

9 Conclusions

In this research paper, a detailed 3D modeling approach was implemented to discretize the structural components of a full-scale RC bridge. The modeling utilized 8-node and 20-node hexahedral finite elements to analyze the nonlinear behavior of RC, rubber, and prestressed concrete. The modeling techniques discussed in this paper are extended to discretize the complete RC bridge. The details of modeling and analyzing the complete bridge are discussed in detail. Cracking was modeled using the smeared crack approach, and a novel technique for modeling post-tensioning systems was introduced. The main objective of this research work was to provide new insight into the computationally demanding modeling approaches through the numerical assessment of a full-scale seismically isolated RC bridge. A detailed model, which incorporated the prestressing cables and a detailed discretization of the standard reinforced elastomeric bearings, was developed on ReConAn FEA using a standard CPU system. The most important findings of the presented numerical investigations are summarized below:

- The developed algorithm met the strenuous computational demands of 3D detailed FE modeling. This finding highlights the importance of optimal algorithmic design and efficient numerical tools, which alleviate computational burdens.
- Based on the results of the parametric investigation, the optimal material parameters for modeling the bridge`s elastomeric bearings were determined. A total of 8 elastomeric bearing models were modeled to be incorporated into the RC bridge mesh.
- A proposed algorithm incorporated the prestressing force into the detailed 3D model, which assigns a post-tensioning force to the tendons (modeled as embedded rebar elements) as an initial force condition.
- Results of the detailed model developed on ReConAn FEA, and the simplified model developed on SAP2000 agreed closely.
- The embedded mesh generation method highlighted the importance of efficient embedded rebar mesh generation techniques, which allocate a large number of embedded rebars inside hexahedral meshes.
- An assessment of the bridge's preliminary design revealed that the elastomeric bearings at the piers were under-designed. Thus, an increase in area was proposed.
- The RC bridge complied with the EC8 code used for seismic assessment. Moreover, the bearings at the piers controlled the numerically projected bridge failure. They were the first structural elements to fail.
- From the deformed shape and cracking pattern, it was deduced that the bridge behaves like a beam under bending. Due to the uneven spans, the deck rotated about the gravity axis (z-axis). The piers cracked at the base due to bending. Also, they developed shear deformations at the heads due to torsional and shear forces caused by the rotation. This type of damage cannot be captured through conventional modeling techniques, which highlights the importance of detailed 3D modeling.
- Prevention of shear cracks at the heads of the piers during an earthquake excitation and an increase in the piers' head diameter is proposed.
- The nonlinear solution was the most computationally demanding, constituting 71% of the total operational time. Writing the output data constituted 26.5% of the total operational time. This demonstrates the computational efficiency of the embedded mesh generation method, which comprises a mere 2.3% of the total analysis time.

- The overall computational response of the software illustrates a novel approach to tackling such numerical problems in a timely manner, given the future advances in both hardware and compiling technologies.
- Future research should incorporate a parallel solution algorithm for the nonlinear analysis, which is the most computationally demanding aspect. Moreover, the soil-structure interaction will be accounted for by discretizing the piling system and surrounding soil. Finally, the embedded rebar element that models the prestressing cables will accommodate the slippage effect.

10 Conflict of Interest Statement

On behalf of all authors, the corresponding author states that there is no conflict of interest.

11 Data Availablity Statement

All data are available from the corresponding author upon reasonable request.

References

[1] CEN, "prEN 1998-2: Eurocode 8: Design of structures for earthquake resistance – Part 2: Bridges," vol. 2, no. 22, 2003.

[2] American Association of State Highway and Transportation Officials., *AASHTO LRFD bridge design specifications : customary U.S. units.*, 4th ed. Washington, D.C. : American Association of State Highway and Transportation Officials, 2007.

[3] R. K. Goel and A. K. Chopra, "Nonlinear Analysis of Ordinary Bridges Crossing Fault-Rupture Zones," *J. Bridg. Eng.*, vol. 14, no. 3, pp. 216–224, May 2009, doi: 10.1061/(ASCE)1084-0702(2009)14:3(216).

[4] A. S. ELNASHAI and D. C. McCLURE, "EFFECT OF MODELLING ASSUMPTIONS AND INPUT MOTION CHARACTERISTICS ON SEISMIC DESIGN PARAMETERS OF RC BRIDGE PIERS," *Earthq. Eng. Struct. Dyn.*, vol. 25, no. 5, pp. 435–463, May 1996, doi: 10.1002/(SICI)1096-9845(199605)25:5<435::AID-EQE562>3.0.CO;2-P.

[5] T. S. Paraskeva, A. J. Kappos, and A. G. Sextos, "Extension of modal pushover analysis to seismic assessment of bridges," *Earthq. Eng. Struct. Dyn.*, vol. 35, no. 10, pp. 1269–1293, Aug. 2006, doi: 10.1002/eqe.582.

[6] A. J. Kappos, M. S. Saiidi, M. N. Aydinoğlu, and T. Isaković, *Seismic Design and Assessment of Bridges*, vol. 21. Dordrecht: Springer Netherlands, 2012.

[7] P. Théoret, B. Massicotte, and D. Conciatori, "Analysis and Design of Straight and Skewed Slab Bridges," *J. Bridg. Eng.*, vol. 17, no. 2, pp. 289–301, Mar. 2012, doi: 10.1061/(ASCE)BE.1943-5592.0000249.

[8] E. T. Filipov, L. A. Fahnestock, J. S. Steelman, J. F. Hajjar, J. M. LaFave, and D. A. Foutch, "Evaluation of quasi-isolated seismic bridge behavior using nonlinear bearing models," *Eng. Struct.*, vol. 49, pp. 168–181, Apr. 2013, doi: 10.1016/j.engstruct.2012.10.011.

[9] I. F. Moschonas and A. J. Kappos, "Assessment of concrete bridges subjected to ground motion with an arbitrary angle of incidence: static and dynamic approach," *Bull. Earthq. Eng.*, vol. 11, no. 2, pp. 581–605, Apr. 2013, doi: 10.1007/s10518-012-9395-2.

[10] A. Abdel-Mohti and G. Pekcan, "Assessment of seismic performance of skew reinforced concrete box girder bridges," *Int. J. Adv. Struct. Eng.*, vol. 5, no. 1, p. 1, 2013, doi: 10.1186/2008-6695-5-1.

[11] T. Potisuk and C. Higgins, "Field Testing and Analysis of CRC Deck Girder Bridges," *J. Bridg. Eng.*, vol. 12, no. 1, pp. 53–63, Jan. 2007, doi: 10.1061/(ASCE)1084-0702(2007)12:1(53).

[12] H. Li, J. Wekezer, and L. Kwasniewski, "Dynamic Response of a Highway Bridge Subjected to Moving Vehicles," *J. Bridg. Eng.*, vol. 13, no. 5, pp. 439–448, Sep. 2008, doi: 10.1061/(ASCE)1084-0702(2008)13:5(439).

[13] N. Johnson, M. S. Saiidi, and D. Sanders, "Nonlinear Earthquake Response Modeling of a Large-Scale Two-Span Concrete Bridge," *J. Bridg. Eng.*, vol. 14, no. 6, pp. 460–471, Nov. 2009, doi: 10.1061/(ASCE)BE.1943-5592.0000009.

[14] W. K. Lee and S. L. Billington, "Modeling Residual Displacements of Concrete Bridge Columns

under Earthquake Loads Using Fiber Elements," *J. Bridg. Eng.*, vol. 15, no. 3, pp. 240–249, May 2010, doi: 10.1061/(ASCE)BE.1943-5592.0000059.

[15] A. Aviram, K. R. Mackie, and B. Stojadinovic, "Nonlinear modeling of bridge structures in California," in *American Concrete Institute, ACI Special Publication*, May 2010, vol. 271, no. 271 SP, pp. 1–26, doi: 10.14359/51663887.

[16] Z.-C. WANG and W.-X. REN, "DYNAMIC ANALYSIS OF PRESTRESSED CONCRETE BOX-GIRDER BRIDGES BY USING THE BEAM SEGMENT FINITE ELEMENT METHOD," *Int. J. Struct. Stab. Dyn.*, vol. 11, no. 02, pp. 379–399, Apr. 2011, doi: 10.1142/S0219455411004142.

[17] P. Kaviani, F. Zareian, and E. Taciroglu, "Seismic behavior of reinforced concrete bridges with skew-angled seat-type abutments," *Eng. Struct.*, vol. 45, pp. 137–150, Dec. 2012, doi: 10.1016/j.engstruct.2012.06.013.

[18] Y. Zhou, J. Prader, J. Weidner, N. Dubbs, F. Moon, and A. E. Aktan, "Structural Identification of a Deteriorated Reinforced Concrete Bridge," *J. Bridg. Eng.*, vol. 17, no. 5, pp. 774–787, Sep. 2012, doi: 10.1061/(ASCE)BE.1943-5592.0000309.

[19] B. Richard, S. Epaillard, C. Cremona, L. Elfgren, and L. Adelaide, "Nonlinear finite element analysis of a 50 years old reinforced concrete trough bridge," *Eng. Struct.*, vol. 32, no. 12, pp. 3899–3910, Dec. 2010, doi: 10.1016/j.engstruct.2010.09.003.

[20] C.-C. Chou, H.-J. Chang, and J. T. Hewes, "Two-plastic-hinge and two dimensional finite element models for post-tensioned precast concrete segmental bridge columns," *Eng. Struct.*, vol. 46, pp. 205–217, Jan. 2013, doi: 10.1016/j.engstruct.2012.07.009.

[21] C. M. FRISSEN, M. HENDRIKS, N. Kaptijn, A. DE BOER, and H. NOSEWIICZ, "3D FEA of Multi-Beam Box Girder Bridges-assessment of Cross-Sectional forces in Joints," *Struct. Eng.*, vol. 38, no. 5, pp. 32–36, 2005.

[22] J. Cervenka, W. Cervenka, and Z. Janda, "Safety assessment of railway bridges by nonlinear analysis," *Bien, Elfgren, Olofsson, editors. Sustainable bridges. Wroclaw: DWE*. 2007.

[23] Z. Sun, B. Si, D. Wang, and X. Guo, "Experimental research and finite element analysis of bridge piers failed in flexure-shear modes," *Earthq. Eng. Eng. Vib.*, vol. 7, no. 4, pp. 403–414, Dec. 2008, doi: 10.1007/s11803-008-1006-5.

[24] V. K. Papanikolaou and A. J. Kappos, "Numerical study of confinement effectiveness in solid and hollow reinforced concrete bridge piers: Analysis results and discussion," *Comput. Struct.*, vol. 87, no. 21–22, pp. 1440–1450, Nov. 2009, doi: 10.1016/j.compstruc.2009.05.005.

[25] T. L. T. Nguyen, P. F. Silva, M. T. Manzari, and A. Belarbi, "System Modeling for Seismic Performance Assessment and Evaluation of Reinforced Concrete Bridge Columns," *ACI*, vol. 271, pp. 125–146, 2010.

[26] Y. Sha and H. Hao, "Nonlinear finite element analysis of barge collision with a single bridge pier," *Eng. Struct.*, vol. 41, pp. 63–76, Aug. 2012, doi: 10.1016/j.engstruct.2012.03.026.

[27] R. Chacón, E. Mirambell, and E. Real, "Strength and ductility of concrete-filled tubular piers of integral bridges," *Eng. Struct.*, vol. 46, pp. 234–246, Jan. 2013, doi: 10.1016/j.engstruct.2012.07.026.

[28] Y. Deng and G. Morcous, "Efficient Prestressed Concrete-Steel Composite Girder for Medium-Span Bridges. II: Finite-Element Analysis and Experimental Investigation," *J. Bridg. Eng.*, vol. 18, no. 12, pp. 1358–1372, Dec. 2013, doi: 10.1061/(ASCE)BE.1943-5592.0000479.

[29] P. Zhu, M. Abe, and Y. Fujino, "Modelling three-dimensional nonlinear seismic performance of elevated bridges with emphasis on pounding of girders," *Earthq. Eng. Struct. Dyn.*, vol. 31, no. 11, pp. 1891–1913, Nov. 2002, doi: 10.1002/eqe.194.

[30] Z. (John) Ma, S. Chaudhury, J. L. Millam, and J. L. Hulsey, "Field Test and 3D FE Modeling of Decked Bulb-Tee Bridges," *J. Bridg. Eng.*, vol. 12, no. 3, pp. 306–314, May 2007, doi: 10.1061/(ASCE)1084-0702(2007)12:3(306).

[31] X. H. He, X. W. Sheng, A. Scanlon, D. G. Linzell, and X. D. Yu, "Skewed concrete box girder bridge static and dynamic testing and analysis," *Eng. Struct.*, vol. 39, pp. 38–49, Jun. 2012, doi: 10.1016/j.engstruct.2012.01.016.

[32] K. Bi and H. Hao, "Numerical simulation of pounding damage to bridge structures under spatially varying ground motions," *Eng. Struct.*, vol. 46, pp. 62–76, Jan. 2013, doi: 10.1016/j.engstruct.2012.07.012.

[33] E. K. C. Tang and H. Hao, "Numerical simulation of a cable-stayed bridge response to blast loads, Part I: Model development and response calculations," *Eng. Struct.*, vol. 32, no. 10, pp. 3180–3192, Oct. 2010, doi: 10.1016/j.engstruct.2010.06.007.

[34] A. Mwafy, O.-S. Kwon, and A. Elnashai, "Seismic assessment of an existing non-seismically designed major bridge-abutment–foundation system," *Eng. Struct.*, vol. 32, no. 8, pp. 2192–2209, Aug. 2010, doi: 10.1016/j.engstruct.2010.03.022.

[35] CSI, "SAP2000 Integrated Software for Structural Analysis and Design." Computers and Structures Inc., Berkeley, California, 2006.

[36] A. Elnashai, V. Papanikolaou, and D. Lee, *ZEUS-NL a system for inelastic analysis of structures*. Urbana (IL): Mid-America Earthquake Center: University of Illinois at Urbana Champaign, 2008.

[37] V. Cervenka, J. Cervenka, and R. Pukl, "ATENA — A tool for engineering analysis of fracture in concrete," *Sadhana*, vol. 27, no. 4, pp. 485–492, Aug. 2002, doi: 10.1007/BF02706996.

[38] LS-DYNA, "LS-DYNA user manual." Livermore Software Technology Corporation, 2007.

[39] S. Lan, J. E. Crawford, and K. B. Morrill, "Design of reinforced concrete columns to resist the effects of suitcase bombs," in *Proc. of 6th Int. conf. on Shock and Impact Loads on Structures*, 2005, pp. 5–10.

[40] "Ansys®, Release 11.0 ,Help System, Ansys documentation, ANSYS, Inc." ANSYS Inc., 2009.

[41] "ABAQUS." Dassault Systèmes® Simulia Corp, United States, 2010.

[42] T. Diana, "Finite Element Analysis User's Manual-Release 9.4.4." TNO DIANA, 2011.

[43] Strand7, "Strand7 FEA software Manual." Strand7 Pty Ltd, 2010.

[44] G. H. Powell and S. D. Campbell, "DRAIN-3DX: Static and dynamic analysis of inelastic 3D structures," University of California, Berkeley, 1993.

[45] F. McKenna, G. L. Fenves, M. H. Scott, and Others, "Open system for earthquake engineering simulation," *Univ. California, Berkeley, CA*, 2000.

[46] "ADINA Theory and Modeling Guide." ADINA R&D, Inc.

[47] "GT STRUDL, Structural Design & Analysis Software."

[48] H. Hartl, "Development of a Continuum-Mechanics-Based Tool for 3D Finite Element Analysis of Reinforced Concrete Structures and Application to Problems of Soil-Structure Interaction," Graz University of Technology, 2002.

[49] M. D. Kotsovos and M. N. Pavlovic, *Structural concrete : finite-element analysis for limit-state design*. Thomas Telford, 1995.

[50] C. Girard and J. Bastien, "Finite-Element Bond-Slip Model for Concrete Columns under Cyclic Loads," *J. Struct. Eng.*, vol. 128, no. 12, pp. 1502–1510, Dec. 2002, doi: 10.1061/(ASCE)0733-9445(2002)128:12(1502).

[51] H. Mirzabozorg and M. Ghaemian, "Nonlinear behavior of mass concrete in three-dimensional problems using a smeared crack approach," *Earthq. Eng. Struct. Dyn.*, vol. 34, no. 3, pp. 247–269, Mar. 2005, doi: 10.1002/eqe.423.

[52] G. C. Lykidis and K. V. Spiliopoulos, "3D Solid Finite-Element Analysis of Cyclically Loaded RC Structures Allowing Embedded Reinforcement Slippage," *J. Struct. Eng.*, vol. 134, no. 4, pp. 629–638, Apr. 2008, doi: 10.1061/(ASCE)0733-9445(2008)134:4(629).

[53] L. Jendele, J. Červenka, V. Saouma, and R. Pukl, "On the choice between discrete or smeared approach in practical structural FE analyses of concrete structures," *Fourth International Conference on Analysis of Discontinuous Deformation Glasgow, Scotland UK*. 2001.

[54] G. Markou and M. Papadrakakis, "An efficient generation method of embedded reinforcement in hexahedral elements for reinforced concrete simulations," *Adv. Eng. Softw.*, vol. 45, no. 1, pp. 175–187, Mar. 2012, doi: 10.1016/j.advengsoft.2011.09.025.

[55] "ReConAn FEA v2.0 User's Manual." 2020.

[56] G. Markou and W. Roeloffze, "Finite Element Modelling of Plain and Reinforced Concrete Specimens with the Kotsovos and Pavlovic Material Model , Smeared Crack Approach and Fine Meshes," *Int. J. Damage Mech.*, vol. 30, no. 6, pp. 845–871, 2020, doi: 10.1177/1056789520986601.

[57] C. D. Newhouse, S. A. Bole, W. Burkett, P. T. Nash, M. El-Shami, and Others, "Study of elastomeric bearings for superelevated U-Beam bridges." Texas Tech University. Center for Multidisciplinary Research in Transportation, 2009.

[58] D. ALLEN, "Stiffness Evaluation of Neoprene Bearing Pads under Long-Term Loads,"

UNIVERSITY OF FLORIDA, 2008.

[59] Australian Standards, “AS 5100.4 SUPP 1-2006 bridge design - bearings and deck joints,” 2006.

[60] J. Wekezer, E. Taft, L. Kwasniewski, and S. Earle, “Investigation of impact factors for FODT bridges. FDOT Structures research laboratory final report,” University of Florida, 2010.

[61] “VSL- CTT Elastomeric Bearings,” 2012. .

[62] B. Bresler and A. C. Scordelis, “Shear Strength of Reinforced Concrete Beams,” *ACI J.*, vol. 60, no. 1, pp. 51–74, 1963.

[63] G. Markou and M. Papadrakakis, “Generating embedded rebar elements for large-scale RC models,” 2013.

[64] G. Markou, “Computational performance of an embedded reinforcement mesh generation method for large-scale RC simulations,” *Int. J. Comput. Methods*, vol. 12, no. 3, pp. 1–41, 2015, doi: 10.1142/S021987621550019X.

[65] G. M. Stavroulakis and M. Papadrakakis, “Advances on the domain decomposition solution of large scale porous media problems,” *Comput. Methods Appl. Mech. Eng.*, vol. 198, no. 21–26, pp. 1935–1945, May 2009, doi: 10.1016/j.cma.2009.01.003.

[66] G. Markou and D. Gravett, “A NEW PARALLEL ALGORITHM FOR THE OPTIMUM EMBEDDED REBAR MESH GENERATION FOR LARGE-SCALE REINFORCED CONCRETE STRUCTURES,” in *8th ECCOMAS Thematic Conference on Computational Methods in Structural Dynamics and Earthquake Engineering*, 2021, pp. 1–9, doi: 10.7712/120121.8771.18591.

[67] F. Abed, H. El-Chabib, and M. AlHamaydeh, “Shear characteristics of GFRP-reinforced concrete deep beams without web reinforcement,” *Journal of Reinforced Plastics and Composites*, vol. 31, no. 16, pp. 1063–1073, Aug. 2012.

[68] AlHamaydeh, M.; Barakat, S.; Abed, F.; “Multiple Regression Modeling of Natural Rubber Seismic-Isolation Systems with Supplemental Viscous Damping for Near-Field Ground Motion,” Journal of Civil Engineering and Management, Vol. 19, No. 5, 2013, pp. 665-682, DOI: 10.3846/13923730.2013.799089.

[69] AlHamaydeh, M.; Choudhary, I.; Assaleh, K.; “Virtual Testing of Buckling-Restrained Braces via Nonlinear AutoRegressive eXogenous Neural Networks,” ASCE, Journal of Computing in Civil Engineering, Vol. 27, No. 6, 2013, pp. 755-768, DOI: 10.1061/(ASCE)CP.1943-5487.0000247.

[70] M.AlHamaydeh, F. Afghan, R. Mithani, T. Besiso, H. Al Salim, “Shear Strength of Circular Beams Made of Geopolymer Concrete and Reinforced with GFRP Rebars,” Proceedings of the International Conference on Smart Sustainable Materials and Technologies (ICSSMT 2020), August 12-13, 2020, AIP Conference Proceedings 2297, 020031; https://doi.org/10.1063/5.0029862 .

[71] M. AlHamaydeh, M. Orabi, “Experimental Quantification of Punching Shear Capacity for Large-Scale GFRP-Reinforced Flat Slabs Made of Synthetic Fiber-Reinforced Self-Compacting Concrete Dataset,” Data in Brief, Vol. 37, No. 5, August 2021, pp. 107196-6. DOI: 10.1016/j.dib.2021.107196.

[72] M. AlHamaydeh, M. Orabi, “Punching Shear Behavior of Synthetic Fiber-Reinforced Self-Consolidating Concrete Flat Slabs with GFRP Bars,” ASCE, Journal of Composites for Construction, Vol. 25, No. 4, 2021, pp. 04021029-16, DOI: 10.1061/(ASCE)CC.1943-5614.0001131.

[73] M. AlHamaydeh, M. Orabi, M. Ahmed, S. Mohamed, A. Jabr, and M. K. Al Hariri, “Punching Shear Capacity of Macro Synthetic Fiber-Reinforced Concrete Two-Way Slabs with GFRP Rebars,” Proceedings of the 11th International Conference on Composite Science and Technology (ICCST-11), pp. 75-80, Sharjah, UAE, April 4-6, 2017.

[74] M. AlHamaydeh, F. Amin, “Data for Interaction Diagrams of Geopolymer FRC Slender Columns with Double-Layer GFRP and Steel Reinforcement,” Data, Vol. 6, No. 5, 2021, pp. 43-49. DOI:10.3390/data6050043.

[75]. Papadrakakis, M., Markou, G. (2022). Assessment of the Structural Response of Steel Reinforced and Steel-Fibre Reinforced Concrete Structures with 3D Detailed Modeling: Limitations and Remedies. In: Aldakheel, F., Hudobivnik, B., Soleimani, M., Wessels, H., Weißenfels, C., Marino, M. (eds) Current Trends and Open Problems in Computational Mechanics. Springer, Cham. https://doi.org/10.1007/978-3-030-87312-7_38.

[76]. Markou, G., Garcia, R., Mourlas, C., Guadagnini, M., Pilakoutas, K. and Papadrakakis, M. (2021), A New Damage Factor for Seismic Assessment of Deficient Bare and FRP-Retrofitted RC Structures, Engineering Structures, 248 (2021), 113152.

[77]. Gravett, Z.D. and Markou, G. (2021), State-of-the-art Investigation of Wind Turbine Structures Founded on Soft Clay by Considering the Soil-Foundation-Structure Interaction Phenomenon – Optimization of Battered RC Piles, Engineering Structures, 235, 112013.

[78]. Markou, G. and Papadrakakis, M., "Accurate and Computationally Efficient 3D Finite Element Modeling of RC Structures", Computers & Concrete, 12 (4), pp. 443-498, 2013.